TEL AVIV UNIVERSITY
RAYMOND AND BEVERLY SACKLER
FACULTY OF EXACT SCIENCES

Detector devlopment for the instruments in the forward region of future linear colliders

Thesis submitted toward the M.Sc. Degree
at Tel Aviv University
School of Physics and Astronomy

by

Itamar Levy

March 5, 2012

The research work for this thesis was carried out in the Particle Physics Department of the Tel Aviv University under the supervision of Prof. **Halina Abramowicz** and Prof. **Aharon Levy**.

Abstract

The design of the luminosity calorimeter (LumiCal) for a future linear collider is based on a tunsten-silicon sandwich calorimeter. The first prototype of the silicon sensor, produced by Hamamatsu, was tested and characterized in the newly set up silicon lab of Tel Aviv University. A sensor equipped with read-out electronics was tested in the 4.5 GeV electron beam of DESY. The results of this first beam-test are presented and indicate that the sensor properties are well understood and that the design of the front-end electronics is adequate.

Contents

Chapter 1

Introduction

1.1 From LHC to LC on the verge of new physics

The strength of the Standard Model (SM) arises, among other qualities, from its general features. During the years, the proof of the SM came from various processes and from various accelerators. Since each machine has its own advantages and disadvantages, they are complementary to each other. The main types of colliders in particle physics are proton-proton, electron-proton and electron-positron colliders.

Nowadays the Large Hadron Collider (LHC) is the machine in the particle physics frontier. The LHC was designed to explore the TeV scale where new physics is expected. It is a proton-proton collider, designed as a discovery machine with up to 14 TeV Center of Mass Energy (CME) in a circular accelerator of about 27 km in circumference. Since its start of operation in 2010, the LHC is running and collecting data at 7 TeV CME. Until the end of 2011 a total luminosity of around 6 fb^{-1} was collected.

Whereas LHC has a high potential for discoveries, an e^+e^- collider will allow precision measurements to explore in detail the mechanism of electroweak symmetry breaking, expected at the TeV scale (as illustrated in Fig. 1.1) . In particular, it would determine the properties of the physics beyond the Standard Model, should it be found at the LHC. A lepton collider provides much cleaner events than a hadron collider. It has the potential to find new particles with hidden signatures which are difficult to see in the complex events of the LHC. Furthermore, the initial conditions of the colliding particles, such as the initial CME and the spin states can be controlled in a lepton collider. Also, in the rather clean events of a lepton collider, missing energy due to particles that are invisible inside the detector, such as neutrinos, will be measured much more precisely. Therefore a high energy e^+e^- linear collider is considered to be the future research facility complementary to the LHC.

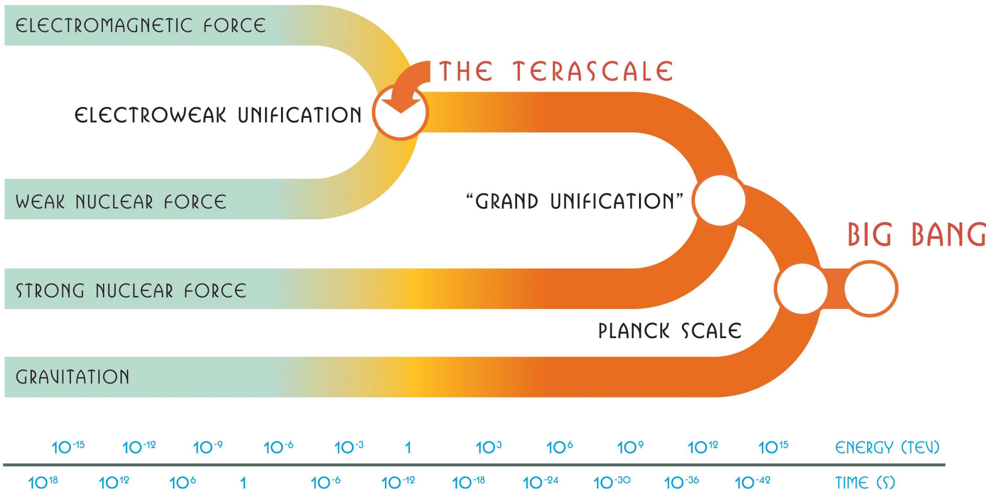

Figure 1.1: A diagrammatic description of the evolution of forces at different energy (time) scales.

Two concepts of an e^+e^- linear collider are presently considered, the International Linear Collider (ILC) and the Compact Linear Collider (CLIC). For the ILC, which uses superconducting cavities, an engineering-design-report will be issued in 2012. The CME will be initially 500 GeV, with the possibility of an upgrade to 1 TeV. CLIC is based on conventional cavities and a novel two-beam accelerating technology. A conceptional design report has been completed in 2011. CLIC will allow to collide electrons and positrons up to energies of 3 TeV.

1.2 LC physics potential

The goal of this section is not to give a comprehensive review of the multitude of existing theories of new physics beyond the SM in the TeV scale. Rather, the goal is to present several reasonable scenarios of new physics and briefly describe the contribution of a high energy e^+e^- linear collider to their investigation. Comprehensive reviews of TeV scale physics, and in particular for the physics case of a high energy e^+e^- linear collider, can be found in reviews like [1] and dedicated reports like [2, 3].

1.2.1 SM Higgs

The experimental successes up to now of the SM, tell us that the standard $SU(2) \times U(1)$ gauge theory describes the interactions of elementary particles to an astounding degree of precision. The model, however, has one glaring flaw - it cannot explain the source of either gauge boson or fermion masses without the existence of an, as yet, unseen scalar particle. This scalar particle is dubbed the Higgs boson. In the minimal version of the model, all particle masses are proportional to a single parameter, the Higgs vacuum expectation value, v, which is determined by muon decays to be $v = 246\,\text{GeV}$. The resulting gauge theory has a single unknown quantity, the mass of the Higgs boson, M_H, and all observables can be calculated in terms of M_H.

The Higgs boson, is the most anticipated discovery from the LHC. In the SM there is only one Higgs particle with a mass that is expected to lie in the range $M_H = 114 - 160\,\text{GeV}$ at the 95% confidence level. This mass estimate was obtained from high-precision data and pre-LHC direct searches [4]. Recent data from the LHC at $7\,\text{TeV}$ continues to restrict the allowed mass range to $M_H = 115 - 131\,\text{GeV}$, as described in [5]. In addition, various theoretical arguments, such as perturbative unitarity, constrain M_H to be smaller than approximately $1\,\text{TeV}$. Thus, such a Higgs particle is expected to be observed at the LHC. The added value of an e^+e^- collider would be to measure in great detail its fundamental properties [3] - its mass and total decay width, its spin-parity quantum numbers, its couplings to fermions and gauge bosons, branching ratios and its self coupling that allows one to reconstruct the scalar potential that is responsible for electroweak symmetry breaking. Some of these measurements are very difficult, if not impossible, in the complicated environment of a hadron machine [6].

1.2.2 Supersymmetry

Supersymmetry is one of the most theoretically motivated extensions of the Standard Model. It is a symmetry of space-time, relating fermions to bosons, and is implemented by associating a new particle differing by one-half unit of spin with every known particle (these particles are collectively dubbed sparticles). Supersymmetric models are very predictive and relate the couplings of the new particles to those of the known particles. This leads to rather generic predictions for the production and decay rates of the sparticles in terms of the unknown sparticle masses.

A theory with unbroken supersymmetry has particles and sparticles of equal mass. Once the supersymmetry is broken, the sparticles obtain masses which differ from their corresponding particles. Since supersymmetric particles are not observed at the weak scale, supersymmetry must be a broken symmetry. Different mechanisms for breaking the supersymmetry lead to varying patterns of sparticle masses [7].

Observing the new particles associated with supersymmetry is a major goal of both the LHC and a linear collider. If supersymmetry is a symmetry at the TeV energy scale, many of the sparticles will probably be discovered at the LHC. However, all of the kinematically allowed sparticles will be produced together, and it will be complicated to distinguish between sparticles and to measured their masses and couplings. The planned e^+e^- collider has the capability to change its center-of-mass energy and so can systematically explore the sparticle spectrum. Since an e^+e^- collider has a well defined initial state, it can distinguish between the sparticles by precision measurement of the mass and spin-parity quantum numbers. In addition, the scalar sparticles associated with the leptons will be easier to observe at a lepton machine like an e^+e^- collider. The precise mass and coupling measurements are crucial to address the fundamental questions about the mechanism of supersymmetry and supersymmetry breaking, about aspects of unification, and about the viability of the lightest supersymmetric particle as a dark matter.

1.2.3 Gauge boson couplings

The measurement of gauge boson self-couplings at a future e^+e^- collider will provide insight into new physics processes in the presence or absence of new particle production. In the absence of particle resonances, and in particular in the absence of a Higgs boson resonance, the measurement of gauge boson couplings will provide a window to the new physics responsible for electroweak symmetry breaking.

An important task is to measure the interactions amongst gauge bosons much more precisely than it was possible at LEP, at the Tevatron and will be at the LHC. For instance, one would like to determine the trilinear self-couplings of the W and Z bosons at the per-mille level. Anomalous values of these couplings are most precisely measured in the clean environment of a e^+e^- collider and at the highest possible CME. The e^+e^- collider thus allows to constrain new physics at scales far above the direct reach of the collider. The measurement of the quartic gauge boson self-couplings is of utmost importance, especially if no Higgs particles have been observed at the LHC and ILC. In this scenario, the interactions between massive gauge bosons become strong at energies close to 1 TeV and the effective scale for the new interactions needed to restore quantum-mechanical unitarity can be extracted from a precise measurement of anomalous values of these self-couplings.

1.3 Work scope

To match the physics benchmarks and objectives required in a high energy e^+e^- linear collider, an R&D program is ongoing to develop the technologies for detectors for precision measurements. The precision is influenced by the knowledge of the beam energy, the absolute luminosity and the beamstrahlung, which affects the average beam energy as well as the effective beam energy spread. The absolute luminosity will be measured by a special instrument in the forward region of the detector. The current development of a forward region instrument prototype for the luminosity measurement is the general subject of this work.

In order to investigate the current development, first the two possibilities for the future high energy e^+e^- linear collider and their detector concepts will be discussed in chapter 2. Then the forward region design and its instruments LumiCal, BeamCal and a Pair Monitor will be presented in chapter 3. The main objective of this work is to study the Silicon (Si)-sensor prototype designed for the luminosity-measurement instrument, LumiCal. The Si-sensor prototype and the lab measurements of its characteristics will be presented in chapter 4. The first use of the prototype in a test-beam will be presented in chapter 5 together with the results of the analysis of the test-beam data.

Chapter 2

Future Linear Cooliders

For the future e^+e^- linear collider, two accelerator concepts are considered at the moment, the International Linear Collider (ILC) based on superconducting cavities, and the Compact Linear Collider (CLIC) with the two-beam concept. The two accelerator share two basic detector concepts, the Silicon Detector (SiD) and the International Large Detector (ILD). This chapter will present a short description of these concepts.

2.1 The ILC project

Over the past decades, studies in Asia, Europe and North America have build the scientific case for a future electron-positron linear collider. A world-wide consensus was formed for a baseline LC project, the International Linear Collider, ILC.

The ILC project is now in mid-term of the technical design phase, started with the publishing of the Reference Design Report (RDR) [3] in 2007. The RDR describes a conceptual baseline design for the ILC, for the global technical design and R&D efforts. The aim of the technical design phase is to have a proof-of-concept for the different elements, to complete the R&D efforts of the key elements, to overcome the problems in industrialization of the key components, and to summarize the efforts in an Engineering Design Report that will serve as the platform for the construction phase.

A snapshot of the current R&D status will be described in a Technical Design Report (TDR), foreseen for this year (the accelerator volume was already published [8] and the physics and detector volume will be published at the end of the year). The TDR represents a major technical progress over the RDR, and presents a significantly more mature design for the ILC.

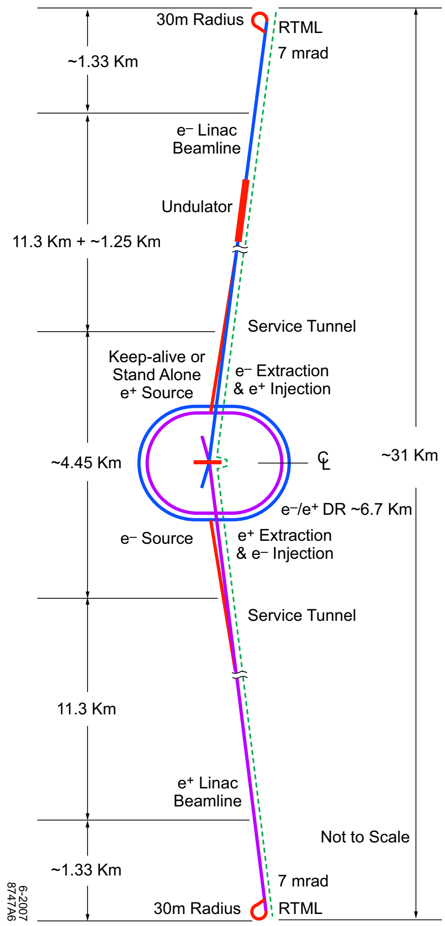

Figure 2.1: Schematic design of the ILC for a CME of $\sqrt{s} = 500\,\mathrm{GeV}$.

The construction cost of the ILC will by strongly affected by the size of the machine. To keep the main linac as short as possible, a high accelerating gradient is needed. The current ILC baseline assumes an average accelerating gradient of 31.5 MV/m in the cavities to achieve a center-of-mass energy of 500 GeV. As seen in Fig. 2.1, that shows its schematic design, these assumptions lead to a 11 km long main linac. In the heart of the accelerator design are the 1.3 GHz superconducting radio-frequency (SCRF) accelerating cavities. The basic element of the technology is a nine-cell 1.3 GHz niobium cavity, shown in Fig. 2.2. About 17,000 such elements are needed for the ILC.

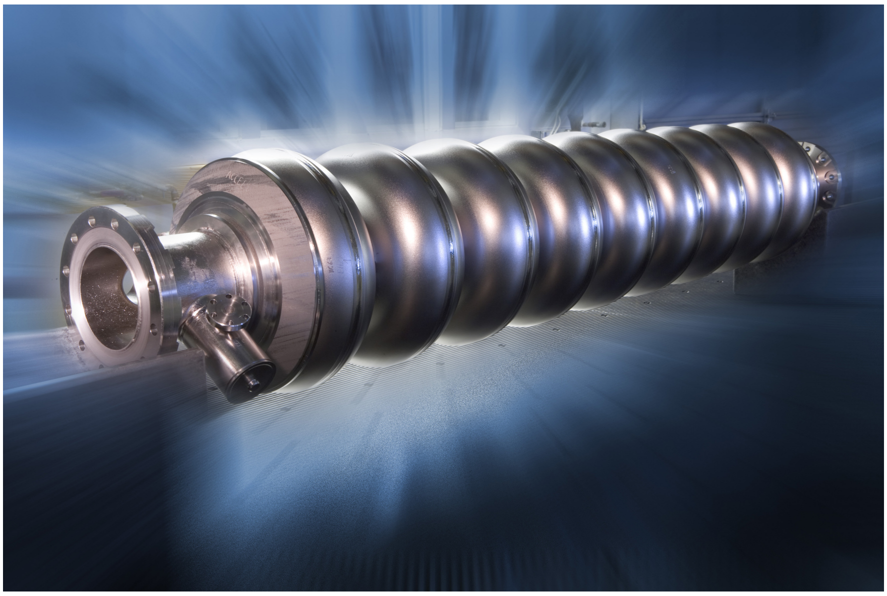

Figure 2.2: The basic nine-cell 1.3 GHz niobium cavity, from ACCEL Corp. in Germany for the ILC [9]

The RDR baseline is designed to achieve the specifications listed in the ILCSC Parameter Subcommittee Report [10]. The three most important requirements are

- ◇ an initial center-of-mass energy, $\sqrt{s}$, of up to 500 GeV, with the ability to upgrade to 1 TeV;
- ◇ a peak luminosity of $2 \cdot 10^{34}\,\mathrm{cm}^{-2}\mathrm{s}^{-1}$ with 75% availability, resulting in an integrated luminosity in the first four years of $500\,\mathrm{fb}^{-1}$ at $\sqrt{s} = 500\,\mathrm{GeV}$, or equivalent at lower energies;
- ◇ the ability to scan the energy range $200 < \sqrt{s} < 500\,\mathrm{GeV}$.

Additional physics requirements are electron (positron) beam polarization $> 80\%$ ($> 50\%$), an energy stability and precision $\leq 0.1\%$, an option for $\sim 60\%$ positron beam polarization, and alternative e^-e^- and $\gamma\gamma$ collisions.

The beam structure is shown in Fig. 2.3. The collider operates at a repetition rate of 5 Hz with a bunch-train length of roughly 1 ms in each repetition. One bunch-train contains 2625 bunches of $\sim 2 \cdot 10^{10}$ particles. The beams are initially accelerated to 5 GeV in low-energy damping rings of

6.7 km in circumference. They are then accelerated in the main linacs, which are $\sim$ 11 km long each, to an energy of 250 GeV. Finally, the beams are focused down to a small spot sizes ($640 \times 5.7\,\mathrm{nm}^2$) at the collision point with a beam delivery system that is $\sim$ 2.2 km long on each side. The total length of the site is $\sim$ 31 km, and will likely be extended for the energy-upgrade to 1 TeV.

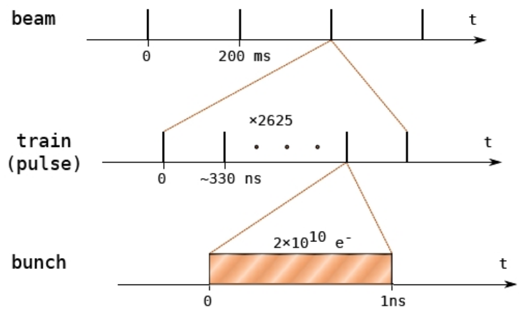

Figure 2.3: The ILC beam structure. Illustration taken from [11].

2.2 The CLIC project

The second accelerator concepts is the Compact Linear Collider (CLIC). The CLIC has a novel accelerating mechanism and a higher planned CME than the ILC. The studies of the CLIC concept continued through the 1990s but got an increased focus and importance with the CERN Council initiative in 2004 to increase the efforts towards producing a Conceptual Design Report (CDR). The Physics-and-Detector volume was published recently [2]. The accelerator volume is expected later this year [12].

The CLIC accelerating mechanism is based on the two-beam accelerator scheme. The 12 GHz RF power is extracted from a low-energy, high-current drive beam, which is decelerated in power-extraction and -transfer structures of low impedance. This power is then directly transferred into the high-impedance structures of the main linac and used to accelerate the high-energy, low-current main beam to energies of 1.5 TeV, which are later brought into collision, resulting in a CME of 3 TeV. The two-beam approach to acceleration offers a solution that avoids the use of a large number of active RF elements in the main linac. In order to limit the overall extension, the scheme is based on average accelerating-gradient of 100 MV/m which results in a total length of 48 km. The CLIC design luminosity is $2 \cdot 10^{34}\,\mathrm{cm}^{-2}\mathrm{s}^{-1}$. A scaled-down design is deduced for lower CME, arbitrarily set at 500 GeV, with the same luminosity for comparison with the alternative ILC technology. The layout of a 3 TeV CLIC is displayed in Fig. 2.4.

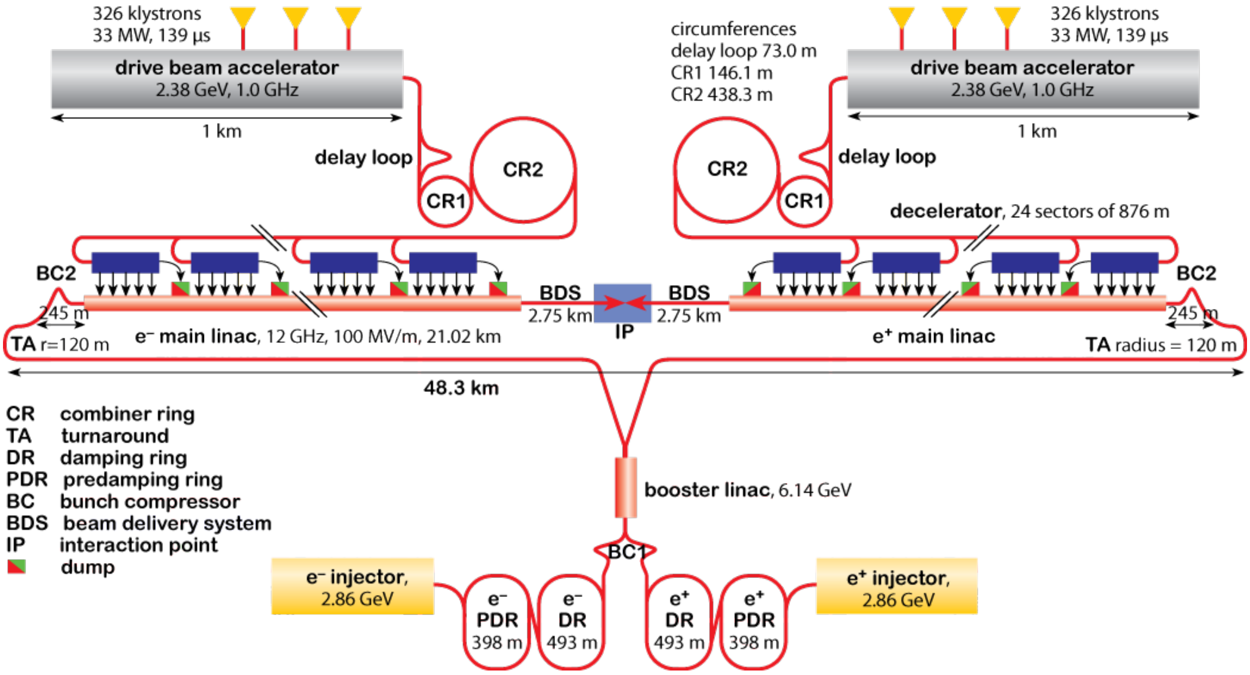

Figure 2.4: Schematic design of the CILC for a center of mass energy $\sqrt{s} =$ 3 TeV.

There are three main aspects of the CLIC machine that determine the physics environment and significantly impact the CLIC detector design.

- ◇ The high bunch charge density, related to the very small beam size ($40 \times 1\,\mathrm{nm}^2$) at the interaction point, means that the electrons and positrons undergo a strong beamstrahlung radiation. Consequently the CME has a long tail towards lower values.
- ◇ There are significant beam related backgrounds. The e^+e^- incoherent pair background has a major impact on the design of the inner region

and the forward region of the detector. The pile-up of approximately 3.2 $\gamma\gamma \rightarrow gg$ mini-jet events per bunch-crossing (BX) impacts the timing requirements placed on the individual detector elements and is an important consideration in all physics analyses.

◇ The CLIC beam consists of bunch trains 156 ns long in a 50 Hz repetition rate. Within a bunch train, the 312 bunches are separated by 0.5 ns and every bunch contains $\sim 3.7 \cdot 10^9$ particles. The short time between bunches means that any detector will inevitably integrate over a number of bunch crossings. This, combined with the significant $\gamma\gamma$ to hadrons background, implies the need for fast readout of all detector elements with excellent time resolution.

2.3 Detector concepts

The physics program of the future e^+e^- linear collider places stringent requirements on the detector performance. These include precise momentum resolution, vertex reconstruction, particle identification, excellent jet reconstruction and hermetic coverage. To allow for flexibility in the beam energy and possible staging of the accelerator, these requirements have to be met over a range of CME. For the ILC, two general purpose detector concepts have been developed into mature designs over the last decade, the International Large Detector (ILD) [13] and the Silicon Detector (SiD) [14]. Both of these concepts were evaluated and validated. They serve as excellent starting points also for the CLIC detectors, with modifications motivated by the more challenging conditions at CLIC. The CLIC detector concepts are usually referred to as CLIC_ILD and CLIC_SiD. A longitudinal cross section of the two concepts, adapted to the CLIC environment, can be seen in Fig. 2.5.

Following the physics requirements, it is not surprising that the main building blocks of the two designs are very similar. Both are cylindrical detectors with tracking and calorimetry inside a solenoid. The two of them share the following main design principles:

◇ very efficient tracking detectors with excellent momentum reconstruction in a high field solenoid;

◇ secondary vertex reconstruction with a powerful pixel detector as close as possible to the beam pipe;

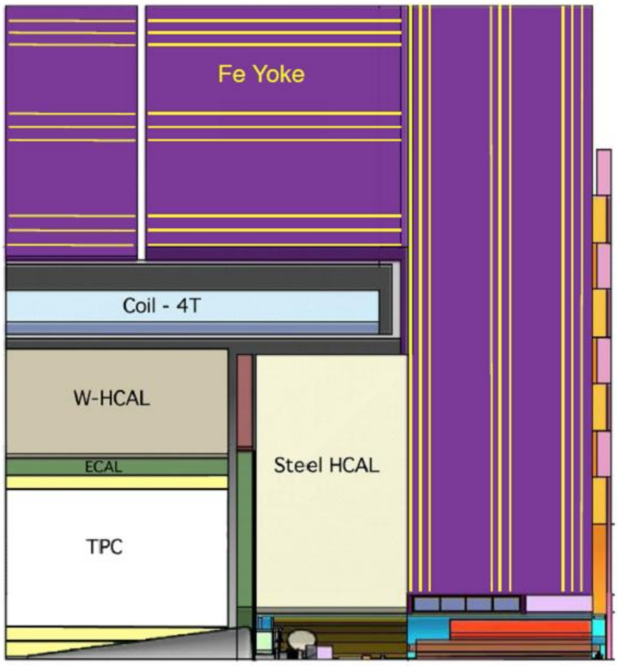

(a)

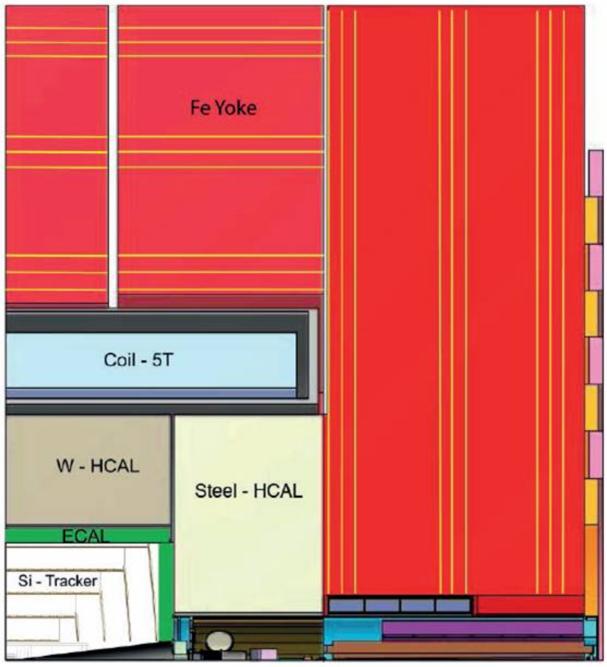

(b)

Figure 2.5: Longitudinal cross section of the top quadrant of (a) CLIC_ILD and (b) CLIC_SiD.

- ◇ low material budgets in the tracking devices;
- ◇ highly segmented electromagnetic and hadronic calorimeters inside the solenoid;
- ◇ Particle Flow Algorithms (PFA) [15] for optimal jet reconstruction define the layout of the detector, in particular for the calorimeters;
- ◇ hermeticity of the detector, crucial for an excellent determination of missing energy which is an important signature for new physics processes;
- ◇ instrumented return yoke for muon identification.

However, particular choices and the overall approach are quite different. The ILD tries to optimize jet reconstruction with calorimetry at large radii to separate the outgoing particles as much as possible at the cost of a lower magnetic field, and with a precision tracking system based on Time Projection Chamber (TPC) which provides up to 200 precise track measurements.

The consequence is an overall radial size like the CMS detector at the LHC. On the other hand, the SiD design is as compact as possible to provide a cost-optimized detector, resulting in a high magnetic field within a solenoid of minimal radius and with precision all-silicon tracking. A comparison of detector concept parameters for both ILC and CLIC is presented in Table 2.1.

Table 2.1: Comparison of detector concepts for ILC (ILD and SiD) and CLIC (CLIC_ILD and CLIC_SiD) parameters.

Concept	ILD	CLIC_ILD	SiD	CLIC_SiD
Tracker	TPC/Silicon	TPC/Silicon	Silicon	Silicon
Solenoid Field (T)	3.5	4	5	5
Solenoid Free Bore (m)	3.3	3.4	2.6	2.7
Solenoid Length (m)	8.0	8.3	6.0	6.5
VTX Inner Radius (mm)	16	31	14	27
ECAL rmin (m)	1.8	1.8	1.3	1.3
ECAL Dr (mm)	172	172	135	135
HCAL Absorber B / E	Fe	W / Fe	Fe	W / Fe
HCAL lI	5.5	7.5	4.8	7.5
Overall Height (m)	14.0	14.0	12.0	14.0
Overall Length (m)	13.2	12.8	11.2	12.8

2.4 Requirements of luminosity measurement

In a e^+e^- linear collider, luminosity, $\mathcal{L}$, is determined by using Bhabha scattering events. The Bhabha scattering is a well-known and theoretically-controlled process. By counting the number of small-angle Bhabha events, N_B, and comparing it to the expected cross section, σ_B, the luminosity can by calculated. The luminosity measurement limit, in this method, is determined by the expected uncertainty on the theoretical cross section and is 5.4×10^{-4}.

In case of the ILC, and even more so at CLIC, the phenomenon of beamstrahlung plays an important role. The beamstrahlung process is the result of the interaction between the charged particles in a bunch with the field generated by the second bunch. At the planned high energies, beamstrahlung causes a significant energy loss and beam energy spread. In general, the collision parameters, that lead to high expected luminosities, also lead to large smearing of the luminosity spectrum. This results in the need to measure the differential luminosity spectrum on top of the integrated luminosity.

The required accuracy of the luminosity measurement is derived from the physics program. At the ILC, the most rigid requirements come from the GigaZ program [16]. This program focuses on the measurement of fundamental parameters from the Z^0 line shape. To fully exploit the GigaZ physics potential, the luminosity uncertainty must be below 2×10^{-4} [17]. Luminosity precision of better than 10^{-3} for the ILC and better than 10^{-2} for CLIC, is essential to study processes like $e^+e^- \rightarrow W^+W^-$ and fermion production, $e^+e^- \rightarrow f^+f^-$. The cross section of the W pair production is strongly forward peaked, and a precise luminosity measurement is needed to probe anomalies in the electroweak $e\nu W$ couplings. The process $e^+e^- \rightarrow f^+f^-$ is sensitive to new physics at very high energy scales via interference with the SM amplitude. To detect deviation from the SM, precise cross section measurements are necessary.

To achieve a precise determination of the Bhabha events rates, a good position and energy resolution is needed. In the future e^+e^- linear collider, in both detector concepts, the luminosity measurement is performed through specially designed instruments in the forward region. The forward region layout and instruments will be discussed in the next chapter, The forward region .

Chapter 3

The forward region

In both detector concepts discussed in section 2.3, two specialized calorimeters are foreseen in the very forward region, LumiCal for the precise measurement of the luminosity and BeamCal for a fast estimate of the luminosity and for the control of beam parameters. To support beam-tuning an additional pair-monitor will be positioned just in front of BeamCal.

The design of the forward region is complicated by the small crossing angle of the two beams and thus the design of the forward detectors is somewhat different for the ILC and for CLIC, as summarized in Table 3.1. Both calorimeters will also improve the hermeticity of the main detector at very small polar angles. For example, in the ILC case, BeamCal covers polar angles between 5 and 40 mrad and LumiCal between 31 and 77 mrad. LumiCal and BeamCal are cylindrical electromagnetic calorimeters, centered around the outgoing beam. In the ILC, LumiCal is positioned inside and aligned with the forward electromagnetic calorimeter (ECAL), while in the CLIC design, LumiCal is positioned just behind ECAL. BeamCal is positioned just in front the final focus quadrupole QD0. The LHCal in the ILC case stands between LumiCal and BeamCal and is meant to extend the coverage of the hadronic calorimeter (HCAL) in the end-cap to smaller polar angles. The forward region layout foreseen for the ILC is shown in Fig. 3.1. The R&D and optimization of the very forward region and its instrumentation is performed by the FCAL Collaboration [18].

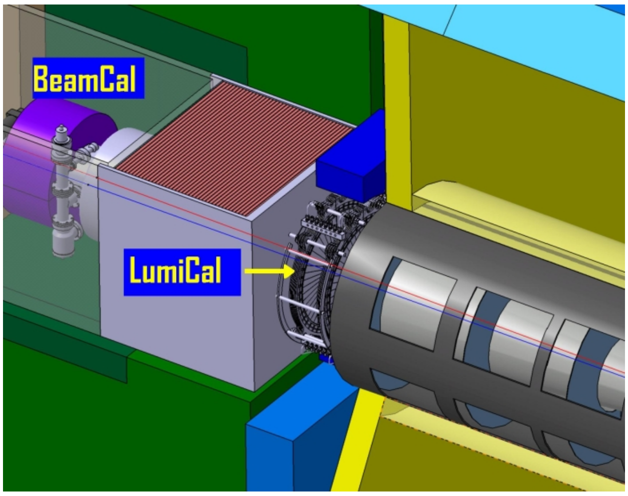

Figure 3.1: Layout of BeamCal and LumiCal in the ILC forward-region design.

Table 3.1: Comparison of the LumiCal and BeamCal designs in the ILC and in CLIC.

		ILC(ILD)	CLIC_ILD
LumiCal	geometrical acceptance [mrad]	31 - 77	38 - 110
	fiducial acceptance [mrad]	41 - 67	44 - 80
	z (start from IP) [mm]	2450	2654
	number of layers (W + Si)	30	40
BeamCal	geometrical acceptance [mrad]	5 - 40	10 - 40
	z (start from IP) [mm]	3600	3281
	number of layers (W + sensor)	30	40
	graphite layer thickness [mm]	100	100

3.1 BeamCal

The BeamCal calorimeter serves three major goals, improving the detector hermeticity down to polar angles of a few mrad, reducing the back-scattering from low-energy e^+e^- pairs into the inner detector part as well as protecting the final magnet of the beam delivery system, and finally assisting in beam diagnostics by detailed analysis of the shape of the pair energy deposition.

BeamCal is designed as a solid-state sensor-tungsten sandwich-calorimeter with tungsten as absorber as illustrated in Fig. 3.2a. BeamCal covers the polar angle range between 5 and 40 mrad. The tungsten absorber-disks will be one radiation-length thick and interspersed with thin sensor-layers equipped with front-end electronics positioned at the outer radius. In front of BeamCal, a 5 cm thick graphite block will be placed to absorb low energy back-scattered particles.

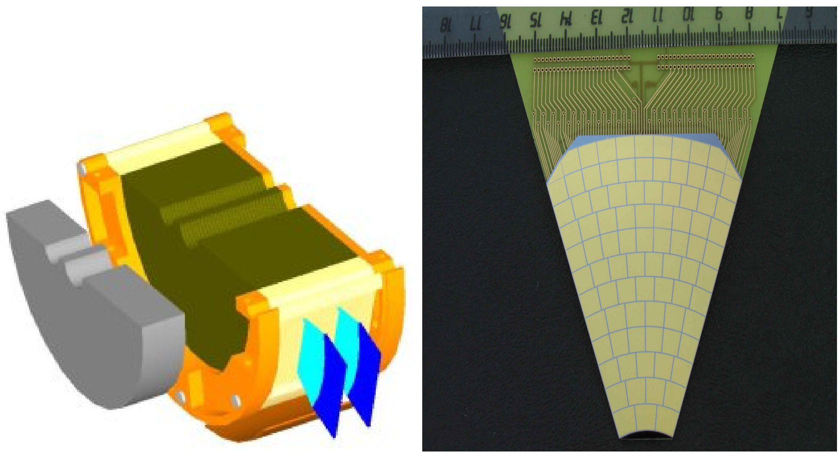

(a) (b)

Figure 3.2: (a) A half-cylinder of BeamCal. The brown block is the tungsten absorber structure interspersed with sensor layers. The orange structure represents the mechanical frame. The blue segments at the outer radius indicate the front-end electronics. In front of the calorimeter a graphite shield, shown in grey, reduces the amount of low energy particles back-scattered into the tracking detectors. (b) One of the GaAs-sensor prototype for BeamCal.

Due to the BeamCal location, the biggest challenge in its design is the development of radiation-hard sensors, that can withstand radiation doses of up to 10 MGy per year. Polycrystalline CVD diamond-sensors of 1 cm^2 size, and larger sectors of GaAs pad-sensors (with pad sizes varying from $4 \times 4\,\mathrm{mm}^2$ to $8 \times 8\,\mathrm{mm}^2$) as shown in Fig. 3.2b have been studied. Since large area CVD diamond-sensors are still very expensive, they might be used only in the innermost part of BeamCal. At larger radii, GaAs-sensors seem to be a promising option.

BeamCal will be hit after each bunch crossing by a large number of beamstrahlung pairs. The total energy, up to several TeV per bunch crossing, and the shape of these deposits allow a bunch-by-bunch luminosity estimate and the determination of beam parameters to be extracted [19]. However, deposits of single high energy electrons must be detected on top of the wider spread beamstrahlung. By using an appropriate subtraction of the pair deposits and a shower finding algorithm which takes into account the longitudinal shower profile, the deposits of the high energy electron can be detected with high efficiency and modest energy resolution, sufficient to suppress the background from two-photon processes in a search e.g. for supersymmetric τ-leptons [20] in certain scenarios.

3.2 Pair Monitor

Additional and independent information on beam parameters will be obtained from the pair monitor. The pair monitor consists of one layer of silicon-pixel sensors, with pixel size of $400 \times 400\,\mu\text{m}^2$ just in front of BeamCal, to measure the distribution of the number of beamstrahlung pairs.

In Fig. 3.3, the pair monitor located in front of the first layer of BeamCal can be seen. Monte Carlo simulation has shown that the pair monitor will give essential information for beam tuning. For example, after averaging over several bunch crossings, the beam sizes at the interaction point can be reconstructed with percent precision [21]. A special ASIC, also shown in Fig. 3.3, is presently developed for the pair monitor. At a later stage, the pixel sensor and the ASIC will be embedded in the same wafer.

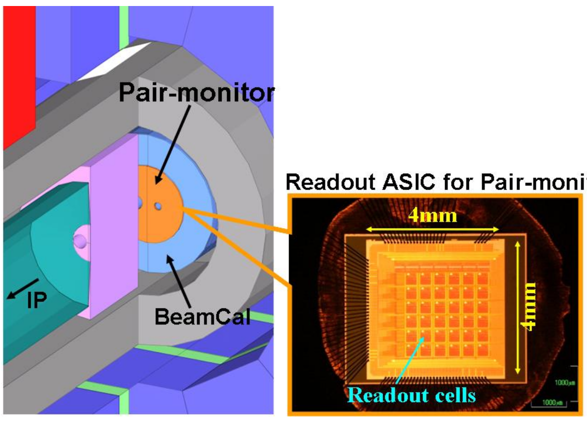

Figure 3.3: The pair monitor located at the first layer of BeamCal with its readout ASIC.

3.3 LumiCal

The LumiCal calorimeter serves (also) three major purposes, measuring the rate of Bhabha scattering events at low angles for precise determination of the luminosity, reducing background by acting as a mask and improving the hermeticity of the detector by providing electron and photon identification down to low polar angles. The main challenge in LumiCal design is to achieve the desired precision of 10^{-4} at the ILC (10^{-3} at CLIC). The precise determination of luminosity requires an excellent knowledge (with tolerance of a few μm) of the lower angular acceptance range of the calorimeter. A laser based position-monitoring system is under development for LumiCal to meet the precision requirement.

Monte Carlo studies have shown that a compact silicon-tungsten sandwich calorimeter is an adequate technology for LumiCal [22]. In the current design for ILC [23], as sketched in Fig. 3.4, LumiCal covers the polar angular range between 31 and 77 mrad. The 30 layers of tungsten absorbers are interspersed with silicon-sensor planes. The front-end and Analog-to-digital-converter (ADC) ASICs are positioned on the outer radius in the space between the tungsten disks. The small Moliere radius (1.1 cm) and finely radially segmented silicon-pad sensors ensure an efficient selection of Bhabha events and a precise shower position measurement [23].

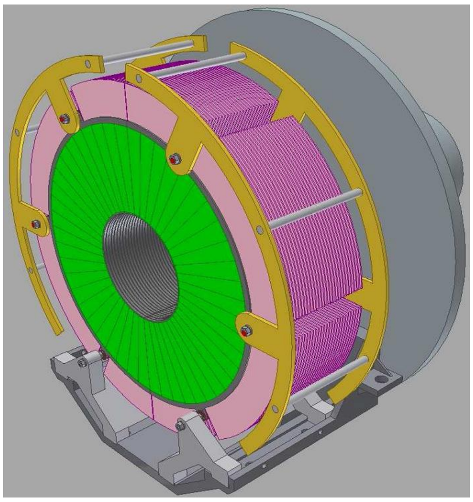

Figure 3.4: Mechanical structure of LumiCal.

A first batch of prototype Si-sensors has been delivered by Hamamatsu

Corporation. The characterization and qualification of Si-sensors in test-bench and after instrumentation with front-end electronics in the test-beam is the subject of the work described in the next chapters.

Chapter 4

LumiCal sensor prototype

R&D studies on LumiCal optimization have allowed to design the detector layout as describe in section 3.3. This led to the design of the layout of the silicon-sensor tiles. The tiles were then custom fabricated by Hamamatsu. As part of the effort to characterize all tiles and in preparation for bonding of the silicon-sensor to the readout chain in the Tel Aviv University (TAU) silicon-laboratory, extensive measurements of sensor Nr 16 have been performed. The measurements include current and capacitance dependence on voltage and time. Temperature and humidity were also recorded. This chapter will presents these investigations.

4.1 Silicon-sensor prototype

As a result of Monte Carlo optimization of sensor granularity, as of today, each of the 30 silicon-layers will be subdivided into 48 sectors ($7.5\,^{\circ}$ each) in the azimuthal direction (around the beam pipe) and into 64 rings in the polar direction (away from the beam pipe). The active area corresponding to this sensor-plane structure extends from 80 mm (inner radius) to 195.2 mm (outer radius) along the detector radius, as shown in Fig. 4.1.

The selection of the sensor type was based on a number of requirements.

- silicon-bulk material - should be n-type, because p^{+}implants in n-material form isolated regions. Other solutions like double layer, are expensive.
- Resistivity of silicon-bulk - as high as possible, because it results in a

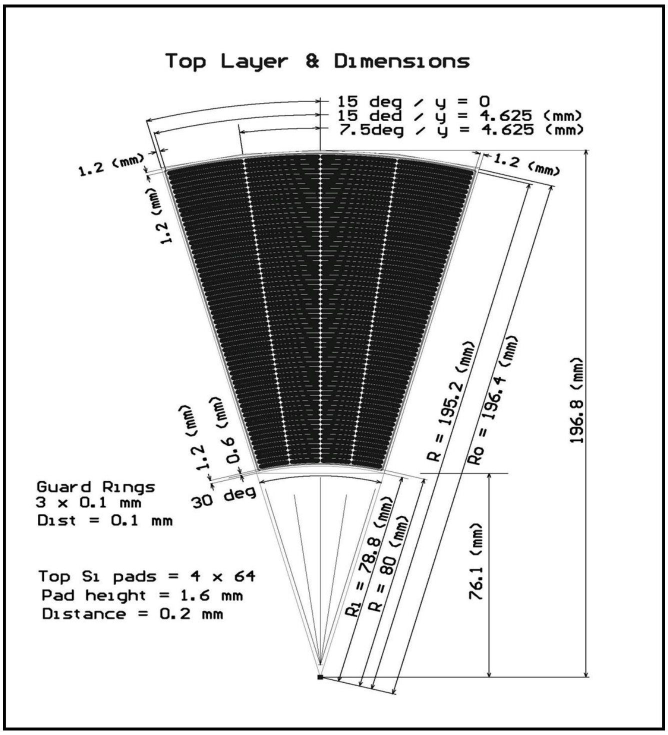

Figure 4.1: The silicon-sensor tile design.

smaller value of depletion voltage and hence smaller power dissipation in the sensor.

- Carrier lifetimes in silicon-bulk - as high as possible, because it results in a smaller value of leakage current leading to a better signal-to-noise-ratio, S/N. S/N, is a common definition that determines how well the signal can by observed above the background noise and influences the resolution of the signal.

- Sensor-thickness - as small as possible, because it results in a smaller value of depletion voltage and a higher value of electric field inside the sensor at a given voltage. This supplies a better charge collection. It also implies less material for particles to traverse and allows to exploit the limited space in the experiment for other purposes.

Knowledge of available silicon-sensor technology, as well as remarks and suggestions from Hamamatsu experts, led to the detailed design of a single tile. These sensor tiles are made of n-type silicon, with p^+strips on n^+back-plane, and have crystal orientation of $\langle$ 100 $\rangle$. They are based on 6-inch wafers technology and each tile contains four azimuthal sectors, which, for 12 tiles completes a full 360° layer. These wafers, which were originally of 500 - 700 μm in thickness, were thinned to 320 μm. The tiles were produced by Hamamatsu in 2009, and one of the sensor-tiles can be seen in more details in Fig. 4.2. The silicon-sensor have the following basic parameters (also seen in more details in Fig. 4.3):

- pad pitch of 1.8 mm;
- pad p$^+$width of 1.6 mm;
- pad Al metalization width of 1.7 mm;
- three guard rings, the presence of which restricts the leakage current from the active sensor area by insulating it from the edge of the sensor.

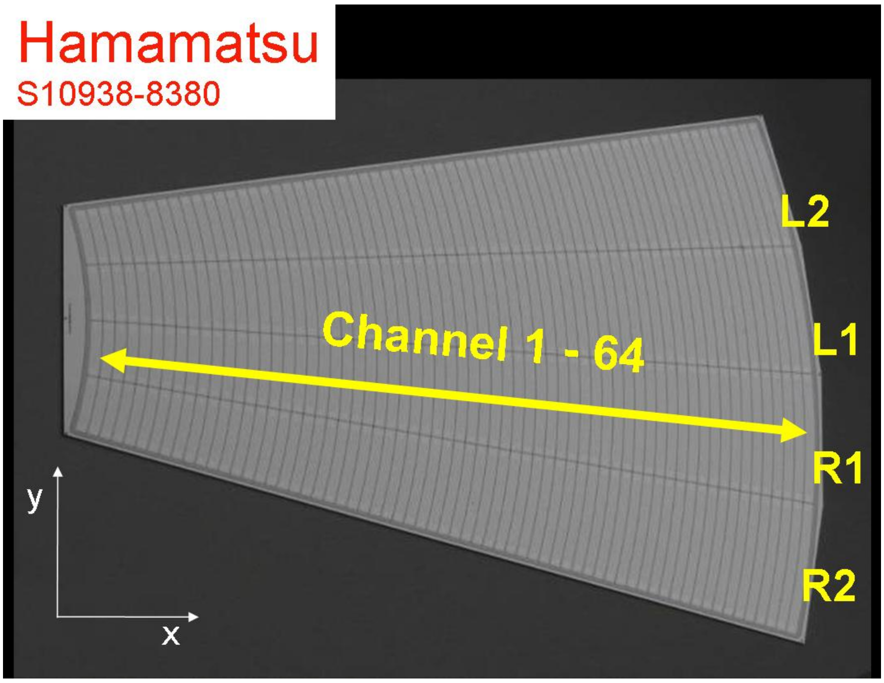

Figure 4.2: The silicon-sensor tile with four sectors, 7.5° opening angle each, and 64 pads in each sector.

In total, Hamamatsu produced 40 such detectors; 20 for IFJ PAN Cracow, 10 for DESY Zeuthen and 10 for Tel Aviv University.

4.1.1 Tile Gap

The mechanical solution of cutting the sensor-tile from a 6-inch wafer (since 18-inch wafers do not yet exist), generates gaps in the active area of each layer. The gap is composed from the mechanical gap (clearance) between tiles designed to be 0.1 mm, the guard rings, which are 0.6 mm wide and a roughly 0.6 mm clearance for wafer cutting. The total inactive gap between tiles has a width of ~ 2.5 mm, as shown in Fig. 4.3 This gap width is taken into consideration in the MC simulations and results in a significant amount of lost signal in the calorimeter. A possible solution to reduce these signal losses is by rotating the odd sensor-layers of the detector by 3.75° with respect to the even layers.

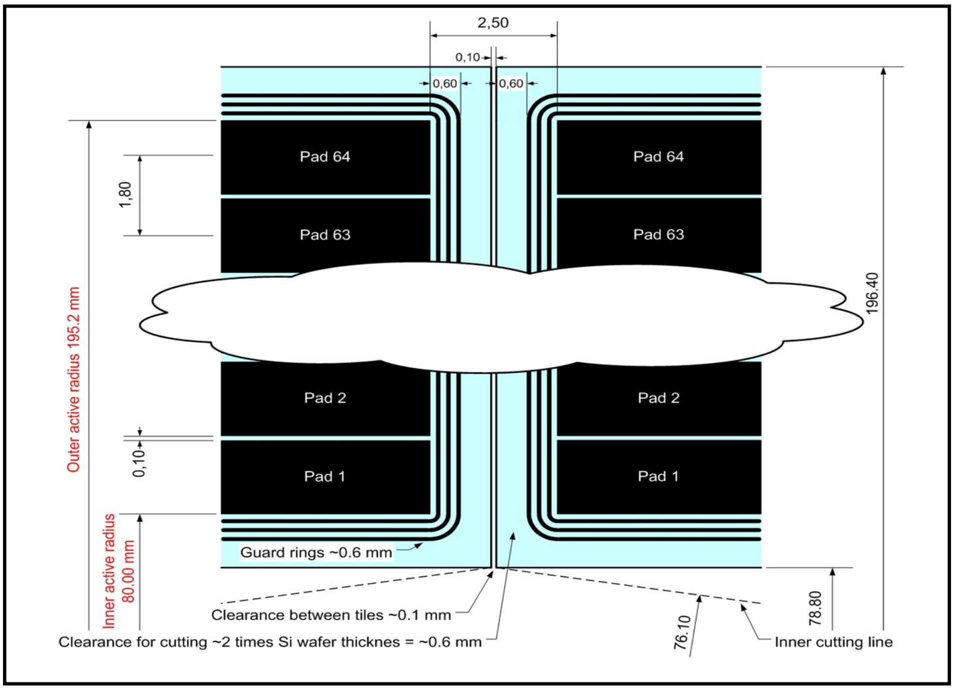

Figure 4.3: A detailed description of the sensor-tile gap. The three guard rings, the pad pitch of 1.8 mm and the 0.1 mm pad gap are also shown.

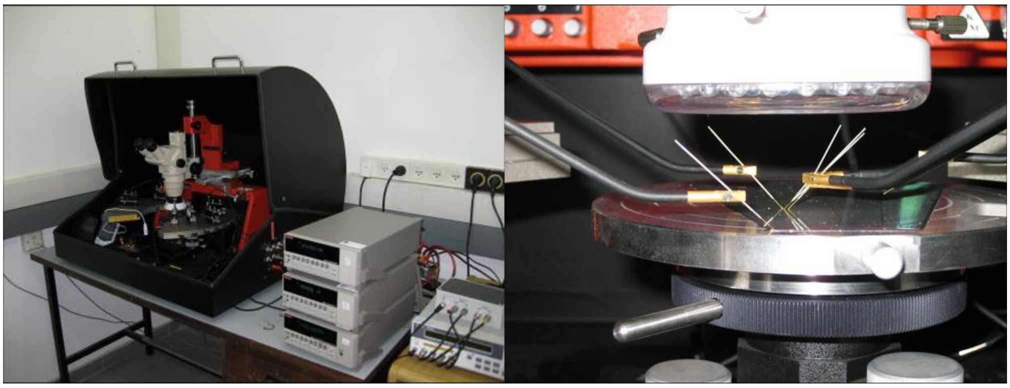

(a) (b)

Figure 4.4: (a) The dark box for sensor measurement with the probe-station inside and the measuring instruments on the right side. (b) Sensor tile in the probe-station.

4.2 Lab measurements of silicon-sensor characteristics

4.2.1 System description and measurement

All sensor measurements were performed with the sensor located in a "dark box" (seen in Fig. 4.4a) that isolated the sensor from light and was also used as a grounded Faraday cage to shield from electromagnetic noise. For each pad, capacitance (C), current (I) and temperature (T) as function of applied voltage (V) or time (t) have been measured; humidity level for each measurement was also recorded.

Special attention was paid to stabilize the measurement system and to understand effects of external conditions. The connection scheme is based on the scheme used by our colleagues from DESY-Zeuthen and Cracow, presented in [24, 25], with some modifications to allow fast and easy swap between the C/V and I/V measurements, as shown in Fig. 4.5.

All measurements were performed with side-neighboring pads in pulse shape formation around the measured pad grounded. The first guard ring was also grounded via the picoammeter. All of the measurement-devices were connected to a DAQ computer via a GPIB connection, and operated through a LabVIEW 8.5 program.

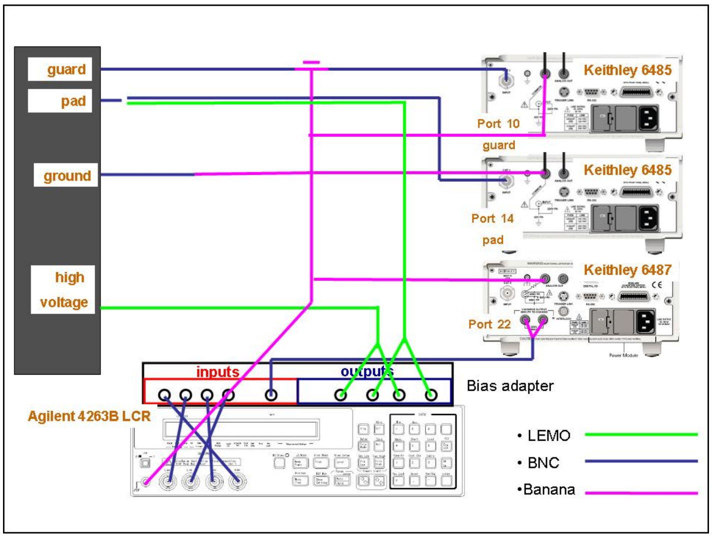

Figure 4.5: Scheme of connections in the lab measurements.

4.2.2 Capacitance measurements

The capacitance characteristics study is important for sensor qualification. The study of the capacitance of all pads is sensitive to the sensor structure and can help find sensor defects. Measurement of the total capacitance of each pad, C_t, has an important role in optimizing the preamplifier design and noise levels. The capacitance between a pad and its neighbor (inter-pad capacitance, C_i) plays a part in the cross-talk between channels. From the capacitance measurements as a function of the voltage, a number of sensor characteristics like the depletion voltage, the depletion width, the donor density and the sensor bulk resistivity, can be inferred.

4.2.2.1 C/V measurement

For the C/V measurement, the dependence of C on the applied V, the Agilent 4263B LCR meter was used. A base voltage in the range of $10 - 150\,\mathrm{V}$ with step size of $\sim 2.5\,\mathrm{V}$ was applied on the sensor through a base adapter. All capacitance measurements were performed with a signal amplitude $U = 1\,\mathrm{V}$ and a signal frequency $f = 10\,\mathrm{kHz}$. Several times a day an "open correction" was preformed to calibrate the LCR meter to subtract the measurement-system capacitance (from wires, adapters etc., of the order of 2.5 pF). Each measurement was saved in a Labview file (.lvm) that contained the date, pad ID, depletion voltage result, temperature and humidity . An example of the C_t measurement as a function of the voltage V, for pads 3 and 60, from all sectors, is shown in Fig. 4.6. In this example, results for two pad-sizes, determined by the polar position (number), are shown. The example shows that pads with the same size in different sectors have the same capacitance, while the bigger pads (pad 60) have a higher capacitance than the smaller ones (pad 3). Since the tile has relatively large pad areas, C_t is mostly a

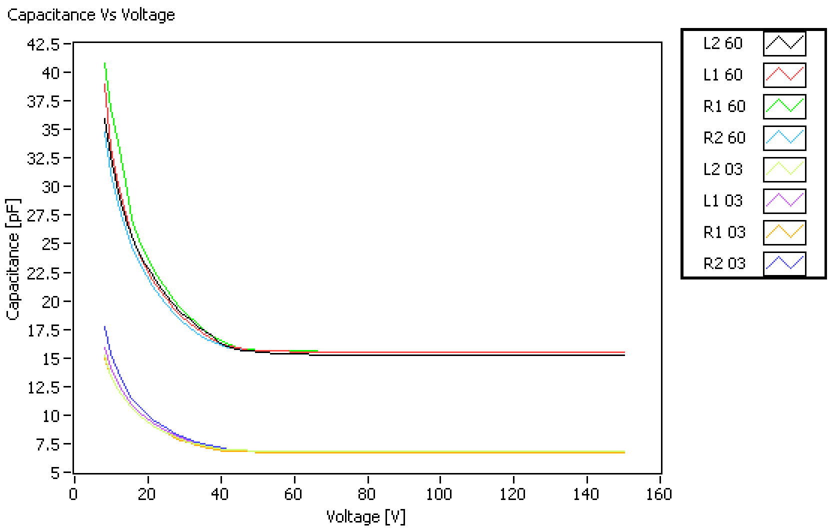

Figure 4.6: The capacitance as function of base voltage for pads 3 (lower curves) and 60 (upper curves), for all four sectors.

geometrical property of the area. Capacitance in a semiconductor diode is created from the accumulated charges on both sides of the depletion layer that acts as a dielectric layer. The geometrical capacitance, C_g, can be assessed within the parallel-plates model with the depletion layer width as the separation between plates. Therefore

$$C_g = A\frac{\varepsilon_{Si}\varepsilon_0}{w} = \begin{cases} A\sqrt{\frac{\varepsilon_{Si}\varepsilon_0 e N_d}{2V}} & \text{for } V < V_d \\ A\frac{\varepsilon_{Si}\varepsilon_0}{w_m} & \text{for } V > V_d, \end{cases} \tag{4.1}$$

where ε_0 is the vacuum permittivity, $\varepsilon_{Si} = 11.68$ is the relative permittivity of Si, A is the pad area, V is the bias voltage, V_d is the depletion voltage, w is the depletion-layer width and is a function of the voltage V, w_m is the maximum depletion-layer width, e is the electron charge, and N_d is donor the density. The behavior described by equation (4.1) is as observed in Fig. 4.6.

4.2.2.2 Depletion voltage

As describe above, the depletion layer width depends on the bias voltage applied to the diode. When the depletion layer width reaches its maximum value, the diode is fully depleted. The maximum width is limited by the thickness of the sensor. The voltage needed to extend the depletion layer to the full thickness of the sensor is denoted by V_d and can be describe by

$$V_d = \frac{eN_d d^2}{2\varepsilon_0 \varepsilon_{Si}}, \tag{4.2}$$

were d is the sensor thickness. In normal operating conditions, only the charge produced in the depleted volume can be detected and therefore the maximal signal charge is achieved when full depletion is reached. In order to determine the sensor operating voltage and to test for problems in sensor-thickness manufacturing, the depletion voltage needs to be determined. It can be determined from equation (4.1) and from Fig. 4.6. It is easier to determine the depletion voltage from the C/V measurement using the $\log(C) - \log(V)$ plot, as shown in Fig. 4.7. For each pad, the depletion voltage was determined as the crossing point between two linear fits in the $\log(C) - \log(V)$ plot. The first linear fit was preformed on the data points with $V < 30\,\mathrm{V}$, and the second fit was done for data points for $V > 80\,\mathrm{V}$.

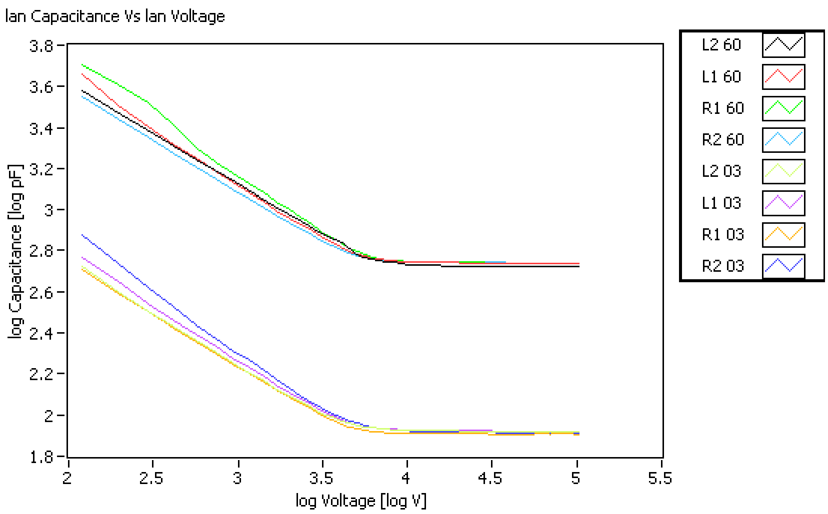

Figure 4.7:
The C/V measurement from Fig. 4.6, shown here in log/log scale. The depletion voltage can be determined from the crossing point of the two linear slopes.

The depletion voltage distribution for all measured pads is shown in Fig. 4.8, resulting in a mean value of 42 V. All measured pads have depletion voltage between $35 - 50$ V.

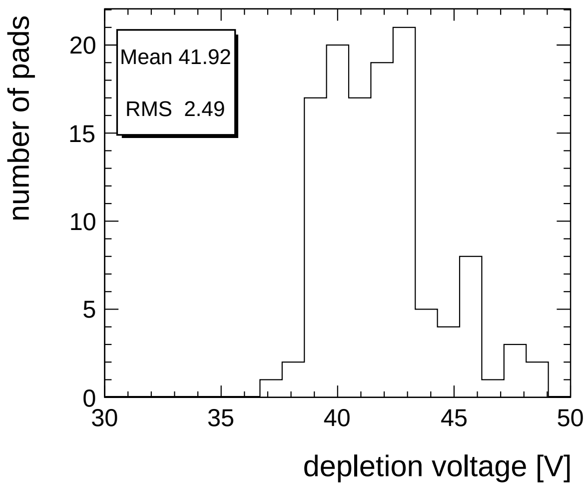

Figure 4.8: The distribution of the depletion voltage for the pads in sensor 16.

4.2.2.3 Donor density and resistivity

The donor density is a characteristic of the n-type silicon-bulk. As seen from equation (4.2), the depletion voltage and width depend on the donor density. Since the dark current of the sensor has a $\frac{1}{\sqrt{N_d}}$ dependence, the total power from the sensor will have depend on N_d as $\sqrt{N_d}$, leading to a requirement of low density. As mentioned at section 4.1, a high resistivity silicon-bulk is one of the requirements of the sensor. The donor density, N_d, is commonly also expressed in terms of resistivity, ρ. The relation between ρ and N_d is

$$\rho = \frac{1}{\mu e N_d}, \tag{4.3}$$

where e is the electron charge and μ is the mobility in the silicon. Since electrons and holes have different mobility, μ is composed of

$$\mu = \mu_e + \mu_p \tag{4.4}$$

with values of [26]

$$\mu_e = 1415 \pm 46 \frac{\mathrm{cm}^2}{\mathrm{Vs}} \quad \text{(for electron)}$$
$$\mu_p = 480 \pm 17 \frac{\mathrm{cm}^2}{\mathrm{Vs}} \quad \text{(for holes).}$$

From the C/V measurements the donor density in the n-type silicon-bulk can by determined. The first part of equation (4.1) can be rewritten as

$$\frac{1}{C^2} = \frac{2}{\varepsilon e N_d A^2} V. \tag{4.5}$$

An example of this relation for the same measurements as shown in Fig. 4.6, can be seen in Fig. 4.9. From the measured slopes one can assess the average of N_d which comes out as $1 \times 10^{12}\ \frac{e}{cm^3}$. This result is similar to that obtained in [24].

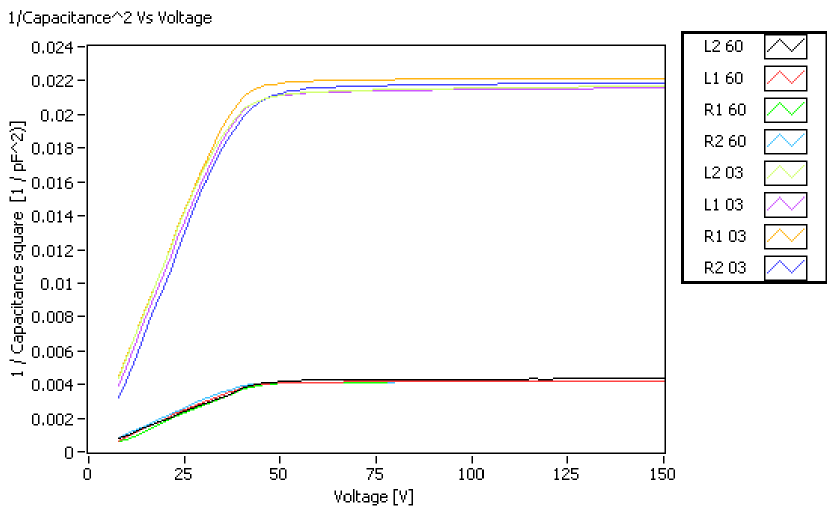

Figure 4.9: The results of the C/V measurement shown in Fig. 4.6 presented as $\frac{1}{C^2}$ as a function of V. The donor density can be determined from the rising slope till the depletion voltage.

4.2.2.4 Final-capacitance estimations

The final-capacitance is the measured value of the C for $V > V_d$. Here we want to compare the measurements of the final-capacitance to the estimated total capacitence, as a function of the pad number (size).

The total capacitance is a sum of the geometric capacitance C_g and the inter-pad capacitance C_i, since, according to [27], they are connected in parallel. As showen in equation (4.1), the final geometric capacitance is determined by the maximum width of the depletion-layer, w_m. As a first order estimate, w_m can be set to d, the sensor-thickness, where for LumiCal $d = 320\,\mu$m. However the p$^+$electrode has some small but non-zero width of some tens of microns. Since the amount of p-doping in the p$^+$electrode is six orders of magnitude higher than the n-doping in the n-type bulk, we can safely assume that the depletion-layer width in the p$^+$side of the junction is negligible. Therefore in order to estimate the full depletion-layer width, only the n-type side is needed. In [28], the estimate of the full depletion-layer width in the n-type silicon bulk is

$$w_m = 0.5[\,\mu\text{m}] \times \sqrt{V_d \rho}. \tag{4.6}$$

Using the result obtained in section 4.2.2.2 for the depletion voltage and in section 4.2.2.3 for the donor density, the full depletion-layer width can be determined from equation (4.6) as $w_m = 220\,\mu$m.

Unlike pixel or strip detectors with small area, in our pad detector the contribution of the inter-pad capacitance in the total capacitance is small. However the inter-pad capacitance is still an important characteristics of the sensor, as it is one of the contributors to the cross-talk between channels. In general, to estimate the inter-pad capacitance, solving a 3D Laplace equation is required. Studies held on this subject, in general, and for the CMS pixel and vertex detector as describe in [29, 27, 30], in particular, found that it is possible to express the inter-strip capacitance per unit of length through the following linearly dependence:

$$C_i = \left[0.03 + 1.62\frac{(d - w_d) + 20\,\mu\text{m}}{p}\right] \text{pF/cm}, \tag{4.7}$$

where $(d - w_d)$ is the p-implants width and p is the pad pitch.

As already stated above, C_i and C_g are connected in parallel and we can sum them up to get the total capacitance of a full-depletion pad. The calculation of each of them depends on the value used for w_m. In the following we will consider two values for w_m, 220 and 320 μm, and calculate the $C - t$ once neglecting the inter-strip capacitance and once by taking it into account. This will be done for pads of different sizes, from the L2 and R2 sectors. In Fig. 4.10, the measured final-capacitance of sensor 16 as a function of pad number (1 is the inner-most pad and 64 is the outer-mos pad) is shown for sectors L2 and R2. A conservative estimate of the measurement uncertainty is 0.3 pF. The measurements are compatible with a linear rise of the final-capacitance with the pad number. The measured values are compared with the calculated total capacitance for the four scenarios mentioned above. The full blue line is for $w_m = 220\,\mu$m and neglecting C_i. When C_i is included, the results are shown with the dotted blue line. The green color is for the case of $w_m = 320\,\mu$m, neglecting (full line) and including (dotted) the values of C_i. The measurements clearly prefer the value of $w_m = 220\,\mu$m. Adding or neglecting C_i has only a minor effect as its contribution to the total capacitance amounts to only about 4%.

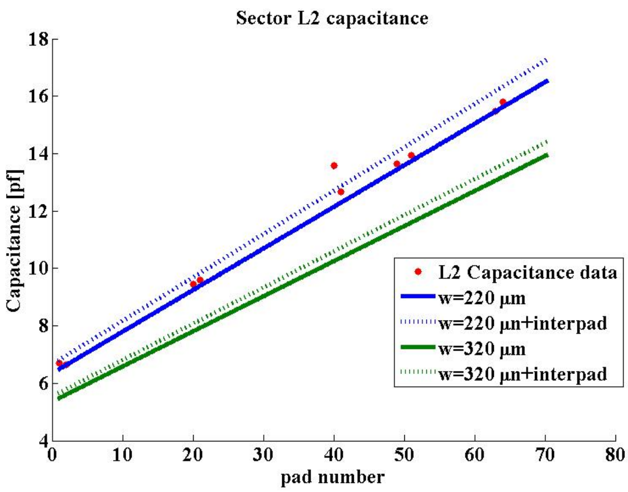

(a)

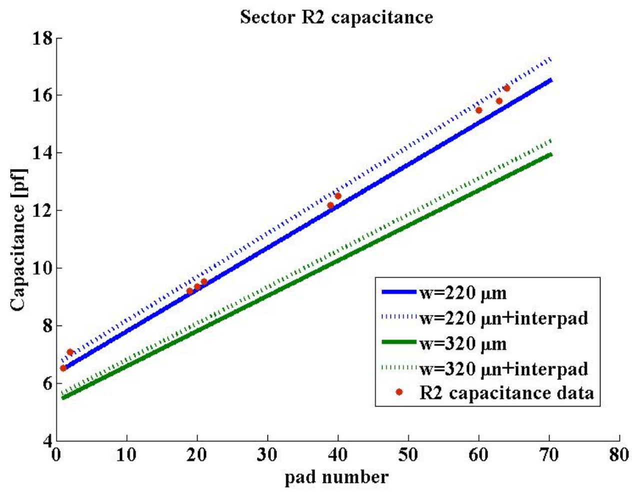

(b)

Figure 4.10: Comparison of capacitance measurements as a function of pad number in sectors L2 (a) and R2 (b) of sensor 16 to theoretical predictions obtained for two depletion widths, 320 μm and 220 μm, with and without C_i contribution, as denoted in the figure.

4.2.3 Current measurement

When a reverse bias is applied to a semiconductor diode, a dark current is created. The leakage or dark current is the current flowing in the absence of external sources, like particles or light that move charges to the conduction band. The source of this current are charges that swap to or are generated in the depletion layer and come out at the other end.

A typical current to voltage characteristic (I dependence on V, traditionally denoted as I/V) of a reversely biased silicon-sensor is composed of three ranges in V. In the first part, for voltage below V_d, the current increases according to equation (4.8). It is proportional to the current density on the surface of the pad, generated in the depletion volume, J_{vol}, which in turn is a function of the intrinsic carrier concentration n_i, and τ_g, the carrier generation lifetime,

$$I_{pad} = AJ_{vol} \approx -eA\frac{n_i}{\tau_g}\sqrt{\frac{2\varepsilon_0\varepsilon_{Si}}{eN_d}V}. \tag{4.8}$$

After the full depletion is reached, the I/V curve displays a plateau region in which the current increase is very small. This part also contains some additional surface-current contribution. At very high voltage, electrical breakdown occurs. This breakdown can eventually destroy the sensor. The measurement of the I/V curves is a very powerful tool for sensor testing. Almost all possible problems in the sensor production process lead to a deviation of the curve from the expected shape.

For the I/V measurement two Keithley 6485 picoammeters were used, one for the pad current measurement and one for the guard current measurement as shown in Fig. 4.5. For reducing the noise level in the pad current, a constant measurement range was set, a slow integration range was chosen and a fast averaging filter was applied in the picoammeter. This procedure reduces the fluctuations in the plateau region of the I/V curve below 0.05 nA. All current measurements were taken in the range of $10-500$ V with ~ 2.5 V steps.

The levels of the current measured were dependent on the system set up. A closer inspection demonstrated that the dark box worked as an antenna for the power-grid, and that there was 12 V AC between the dark box and external ground. The configuration shown in Fig. 4.5 was set after proper grounding of the dark box. Test measurements with two resistors, one of 23.2 MΩ and the other of 198 MΩ were preformed to simulate the measurement of the pad current, I_{pad}, and the guard current, I_{guard}, (see Fig. 4.11) to ensure that the measured levels are correct. From the dependence of V on I, the resistance can be extracted. For the larger resistance, a value of 194 MΩ is obtained, while for the lower resistance it is 23.2 MΩ is extracted. This is well within the 5% inherent uncertainty on the original resistance.

An example of the I/V measurements is presented in Fig. 4.12, with I_{guard} dependence on V shown in (a) as and I_{pad} dependence on V in (b). All the measurements in Fig. 4.12 are for pad number 59 in sector L2 (L2:59), and the various curves are obtained for different ambient temperatures. Both for the guard current and pad current measurements, the lowest curve corre-

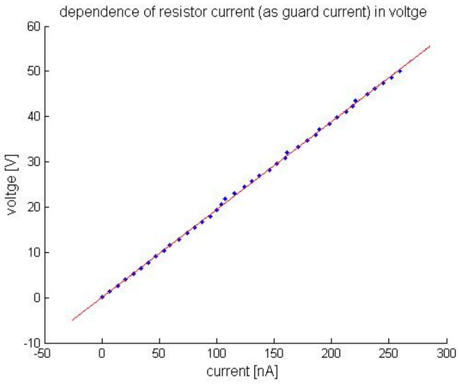

(a) Test for pad current with 23.2 MΩ resistor

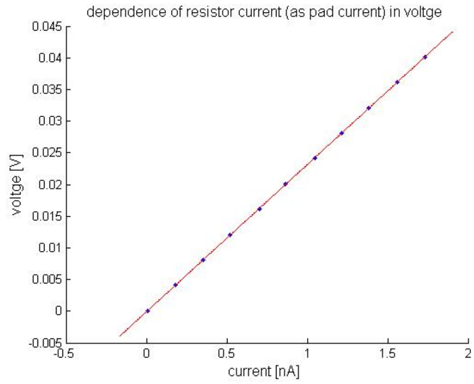

(b) Test for guard current with a 198 MΩ resistor

Figure 4.11: Measurements of voltage as a function of current for a low resistance (a) and a high resistance (b) resistors (dots) as described in the figure. A linear fit to the results is shown with a continuous line.

sponds to the lowest recorded temperature (in black in the figure). In case of the pad current, this particular curve has a V dependence as expected from theoretical considerations. Other curves for pad (L2:59) show a similar behavior but with two notable differences, the current levels are changing and a structure appears at low V, not expected in the theoretical dependence, most probably due to surface and humidity effects. The measured values of the guard current, I_{guard}, and the pad current,I_{pad}, were similar in size but slightly lower than the values measured in the Cracow and in the Zeuthen labs [24, 25]). This is probably due to the strong dependence of the current on temperature and a in general lower temperature during the measurements performed in Tel Aviv (all pads were measured in an ambient temperature of less than 20°).

The temperature dependence arises from the intrinsic carrier concentration, the n_i term in equation (4.8). From the known dependence of n_i on temperature T [31], the following relation may be derived for J_{vol},

$$J_{vol} \propto T^2 e^{\frac{E_g(T)}{2k_B T}}, \tag{4.9}$$

where E_g is the energy gap and k_B is the Boltzmann constant. For $T \simeq 300\,\mathrm{K}$, an increase of temperature by 8 K would cause the dark current to double in value.

The primary observation from the current measurements is a strong dependence of the dark current on the surrounding temperature (inside the

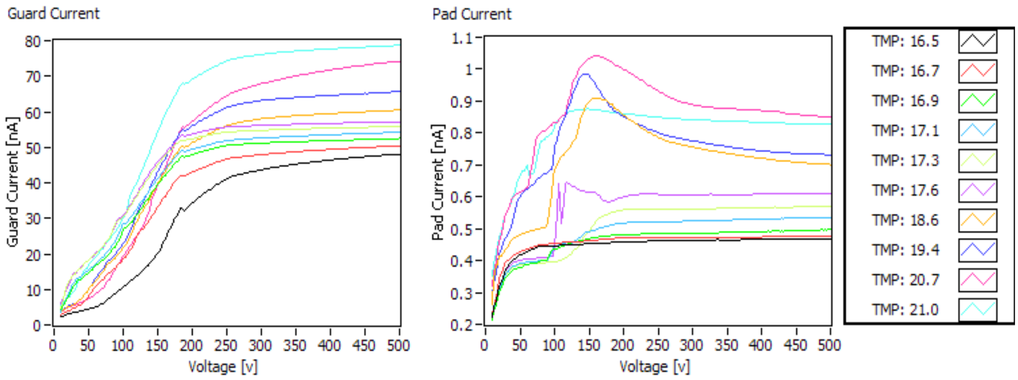

(a) (b)

Figure 4.12: The dependence of the measured dark current on voltage for pad L2:59 and for different ambient temperatures as descibed in the figure for (a) guard current and (b) pad current.

dark box) as seen in Fig. 4.12. To dependence of the dark current, averaged in the range $300 < V < 500\,\mathrm{V}$ on T is shown in Fig. 4.13, for the guard and pad current. All temperatures were measured around the sensor and controlled using the lab air-conditioner. An estimate of this dependence was

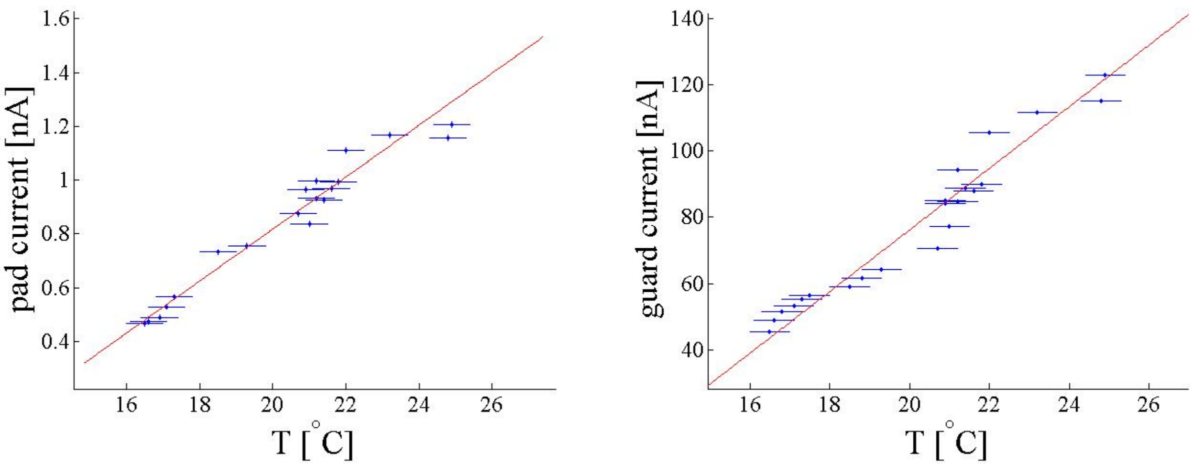

(a) (b)

Figure 4.13: Estimated dark current (dots) averaged in the range $300 < V < 500\,\mathrm{V}$ as a function of temperature, T, for pad current (a) and guard current (b). Also shown is a linear fit (line).

made by performing a linear fit that gave a slope of $0.0968 \pm 0.0005\,\mathrm{nA/^\circ C}$ for the pad current (Fig. 4.13a) and $9.3 \pm 0.05\,\mathrm{nA/^\circ C}$ for the guard current (Fig. 4.13b) .

4.2.4 Temperature effects and stability measurement

As part of the effort to stabilize the measurement system, long current (pad and guard ring) measurements were taken with the sensor kept at constant voltage (100 V). The system was very stable with the current changing with temperature with similar dependence as observed in Fig. 4.13. The other tendency observed in following the current dependence on time as shown in Fig. 4.14 is that while the temperature reaches with time a constant level (also shown in the figure), the currents in the pad and in the guard ring start rising. The rise seen in Fig. 4.14 is of 0.02 nA for the pad current and 2 nA for the guard current over a period of 6 hours. This rise corresponds for both currents to a temperature rise of 0.2°, so the logical explanation seems to point to the self-heating of the sensor, due to the power generated in each pad. Since the ambient temperature is measured at a distance of about 15 cm from the sensor, it may not be sensitive to the local self-heating.

4.2.5 Conclusion

Until now, the measurements of sensor Nr 16 performed at TAU gave similar results to those obtained in the Cracow and the Zeuthen tests for the C/V measurement and for the I/V measurements of the silicon LumiCal prototype sensors. One difference is found in the final pad current levels. All currents are below 1 nA at temperature less then 20°, while in the other labs they are in the range $1-2$ nA. This result is believed to be due to the difference in average temperature between labs and the strong correlation between the current and the temperature as shown in this chapter. Most C/V measurements yield depletion voltage levels of around 41 V, fairly uniform in the sensor plane. The final measured capacitance and the differences between pads correspond to theoretical expectations for this setup. The capacitance measurements allow to evaluate the sensor characteristics, such as the size of the full depletion layer, the sensor resistivity and the number of donor, N_d. A suspected self-heating effect was observed for measurements conducted over long periods of time.

As part of the preparations towards the construction of the LumiCal

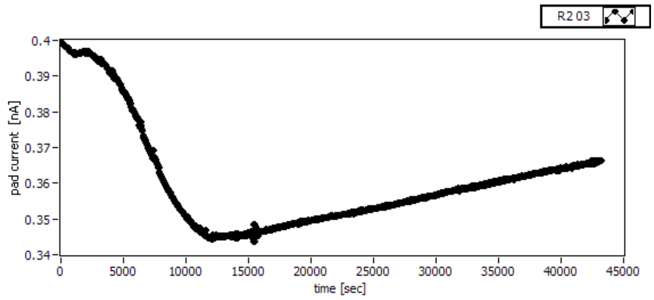

(a) Pad current

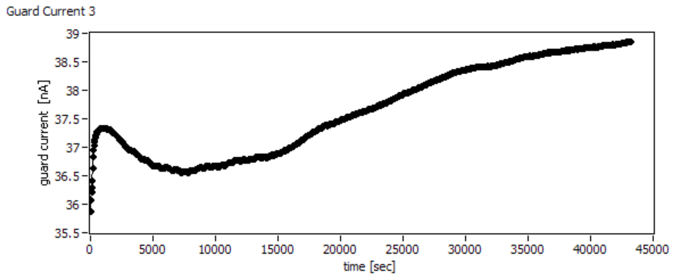

(b) Guarg current

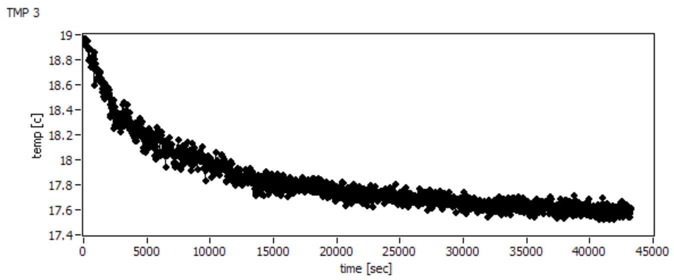

(c) Temperature

Figure 4.14: Time dependence of the measurements of the pad current (a), guarf current (b) and temperature (c) over a period of 12.5 hrs.

prototype within the AIDA (FP7) project, a full characterization of all TAU sensors is needed. The next step will be to bond the sensor to the Kapton fun-out and to the front end electronics (wire bonding/conductive glues) for performance tests of the full chain. Another very important and very well known characteristic of semiconductor sensor is the Charge Collection Efficiency, CCE. The Tel-Aviv particle physics silicon-lab does not have yet the necessary infrastructure for such measurements.

Chapter 5

Tests Beam

In the summer of 2010 the FCAL collaboration performed the first test-beam measurements of the LumiCal silicon- and the BeamCal GaAs-sensors prototypes [32, 33]. In these measurements, the full readout chain, including silicon-sensors, Kapton fan-out and front-end electronics [34], were tested for the first time. This chapter will describe the test-beam setup and the measurements performed in the beam with the LumiCal sensor. An analysis of the measured spectra, of the cross-talk and of the performance of the sensor as a function of hit-position will be presented.

5.1 Test setup

The tests with the beam were performed at the DESY Hamburg facility using a 4.5 GeV electron beam from the DESY-II ring. The tests were held in area 22 that hosts the ZEUS MVD Telescope [35, 36]. This telescope, described in details in subsection 5.1.3, records each beam particle. For each run, data were collected from the MVD Telescope data-acquisition-system (DAQ), and the sensor DAQ see subsection 5.1.4. The two DAQs were running independently of each other, on two different computers and though they had a common trigger, the triggers are not synchronized as described in subsection 5.1.5. The two data streams were recorded in two separate files, one for each DAQ.

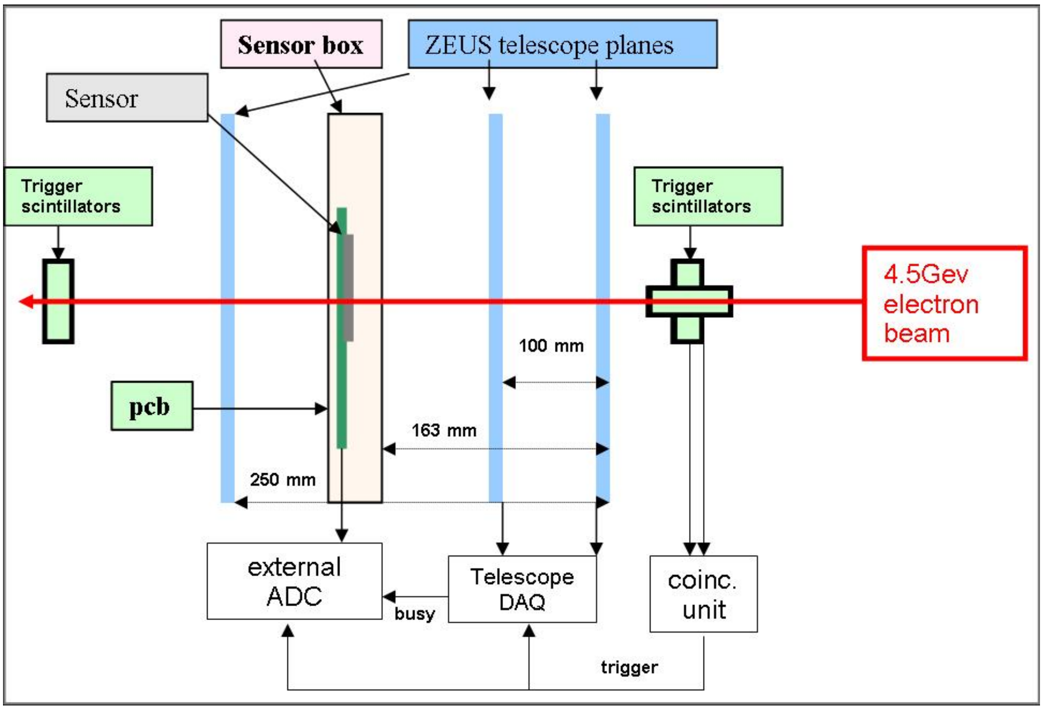

Figure 5.1: The test beam setup, showing the box with the sensor between the second and third telescope planes. The signal connections are also shown.

5.1.1 Beam

The electrons for the beam were provided as illustrated in Fig. 5.2. A bremsstrahlung beam was generated by a 25 μm thick carbon fiber (primary target) in the synchrotron beam in the DESY II ring. A metal plate (secondary target) was used to convert these bremsstrahlung photons into electron and positron pairs. A dipole magnet spread the beam out into a horizontal fan, and a set of collimators formed the extracted beam. The magnet setting was also used to control the energy of the beam. This provided electrons with energies from 1 to 7 GeV. In this range, the electrons have as minimum ionizing partilces (MIP). The bremsstrahlung spectrum has a $1/E$ dependence on energy of the electrons, E. The energy distribution of the electron/positron pair conversion is nearly flat.

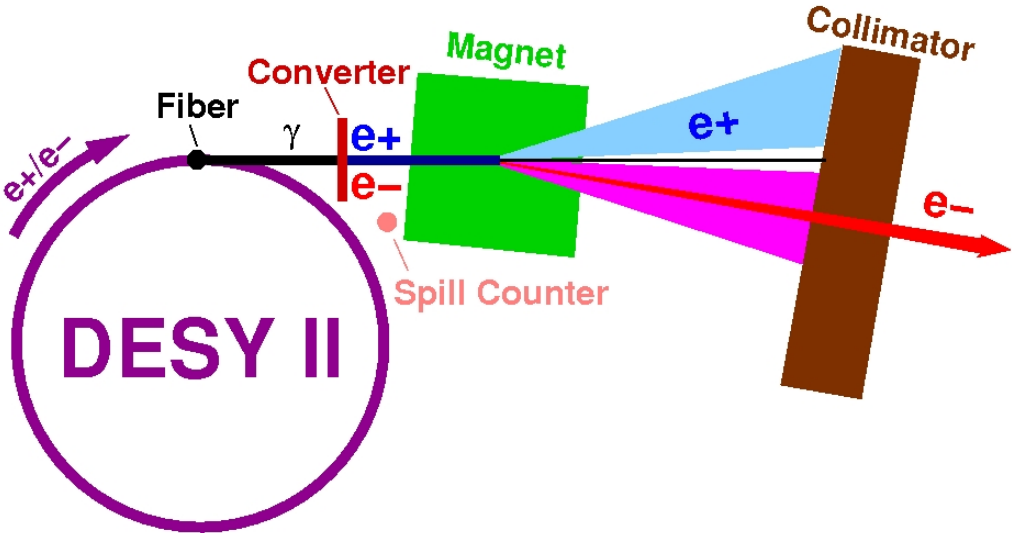

Figure 5.2: Test beam layout.

5.1.2 Rate

In order to understand the data rate it is important to understand the cycle of the machine. The energy of the synchrotron radiation varies with time, with cycles of the accelerator. The synchrotron radiation accelerates and decelerates in a sinusoidal mode with a frequency of 12.5 Hz. One DESY II cycle takes 80 ms as shown in Fig. 5.3 and thus the beam can reach the test area only when the accelerator energy is above a chosen momentum, selected by the beam-extracting magnet. As will be discussed in subsection 5.1.5 the event-record rate depends on the slowest DAQ system. Since the beam momentum is changing sinusoidally, the beam above a certain threshold will reach the test area only in part of the period. So the real rate in which events are written on disk ends up being a product of the slowest DAQ rate and of the relative fraction of time in which the beam-momentum is higher than the chosen threshold. The slow-down was particularly significant in the 2011 tests, when the sensor DAQ could handle a maximum rate of about 150 Hz.

5.1.3 The ZEUS MVD Telescope

The beam telescope was originally assembled for the beam tests of the ZEUS micorvertex detector (MVD) [35, 36]. The telescope consists of three modules, each containing two perpendicular layers of silicon-strip detectors. Hence, each module provides the x, y and z coordinates which can be used for beam-

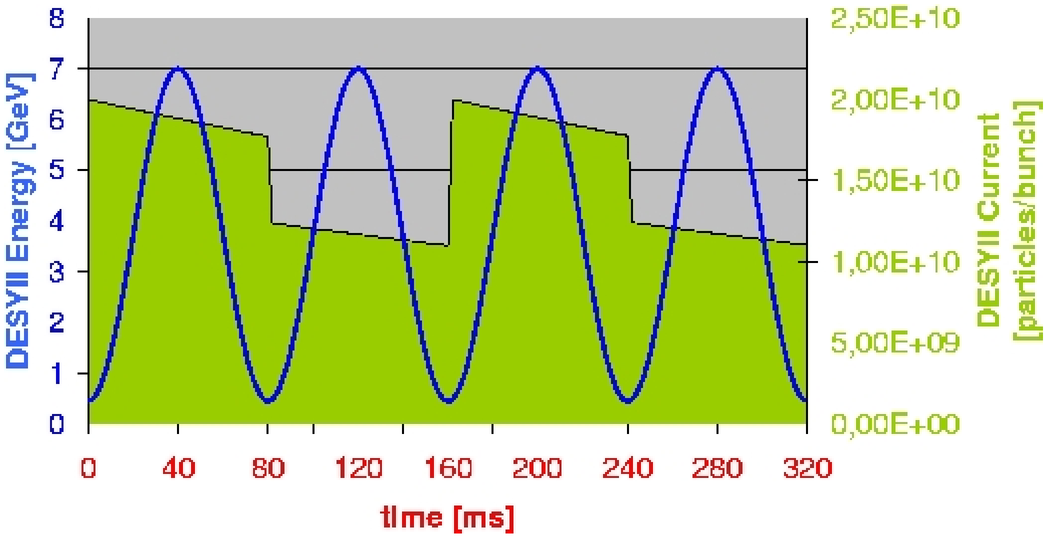

Figure 5.3: Beam energy and ring current as function of time and accelerator magnet oscillations.

track reconstruction to predict the impact position on the device under test (DUT). Each layer consists of a single-sided silicon strip detector, 300 μm thick and $32 \times 32\,\text{mm}^2$ in area. The strip pitch is 25 μm and the readout pitch is 50 μm. The 640 readout strips on each sensor are read out by the VA2 chips (VA2 chip is a product of IDE AS, Norway, described in [37]). All modules have a very good signal-to-noise (S/N) ratio for a MIP, $80 \leq S/N \leq 130$ and a high intrinsic position resolution of 28 μm [38].

To study the performance of the LumiCal sensor tile as a function of position, the sensor box (DUT) was put between the second and the third planes of the ZEUS MVD telescope, as shown in Fig. 5.1. The DUT was set up on a remotely-controlled precision table in the xy-plane (the beam was along the z-axis), which allowed the DUT to be moved in the beam. The xy-table itself was mounted on the same optical bench as the telescope.

5.1.4 The DUT and DAQ

The DUT, or sensor box, was prepared before arrival at the test-beam site. A dedicated PCB was developed, produced and mounted within the shielded box. The PCB contained the front-end ASICs, the power supply and biasing circuits, the output buffers, and one tile of silicon-sensor as shown in Fig. 5.4. The silicon-sensor was glued to the main board using conductive

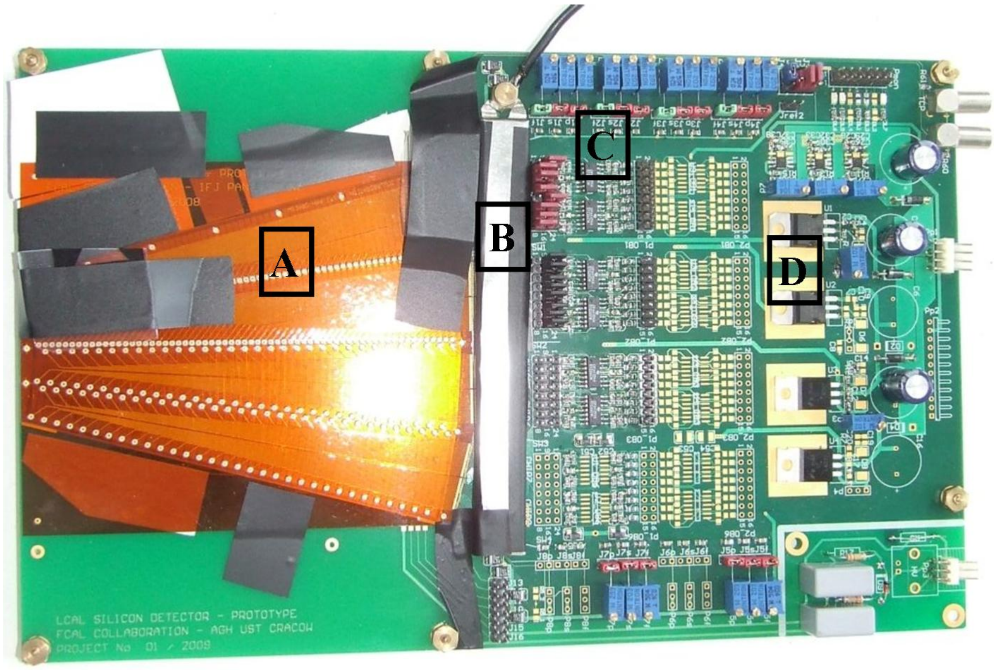

Figure 5.4: The full PCB board including the sensor tile and the electric board. A - silicon-sensor bonded to the Kapton fan-out; B - 5 ASIC's chips (covered by a metal plate); C - line drivers; D - the power supply and biasing circuits

glue and covered by Kapton fan-out. The fan-out provided connections between the sensor and the front-end electronics (8 channels) by wire bonding. Analogue signals were driven out of the box and sent to an external sampling ADC (v1724, 14 bit, 100 Msps) provided by CAEN. The v1724 was read and controlled by the DAQ C++ software that was adapted from the fast-beam-condition-monitor of the CMS experiment. At trigger time, the available 8 channels were recorded with 128 samplings, 10 ns apart, as shown in Fig. 5.5.

5.1.5 Trigger logic

Two scintillators in front of and one in the back of the telescope (see Fig. 5.1) in coincidence provided the trigger signal for the system. As the readout time for the telescope was ~ 1 ms and for the DAQ $\sim 1\,\mu$s, a synchronization between the different DAQs was needed. Since the data were collected in two different DAQs, the information from the telescope and the DUT had

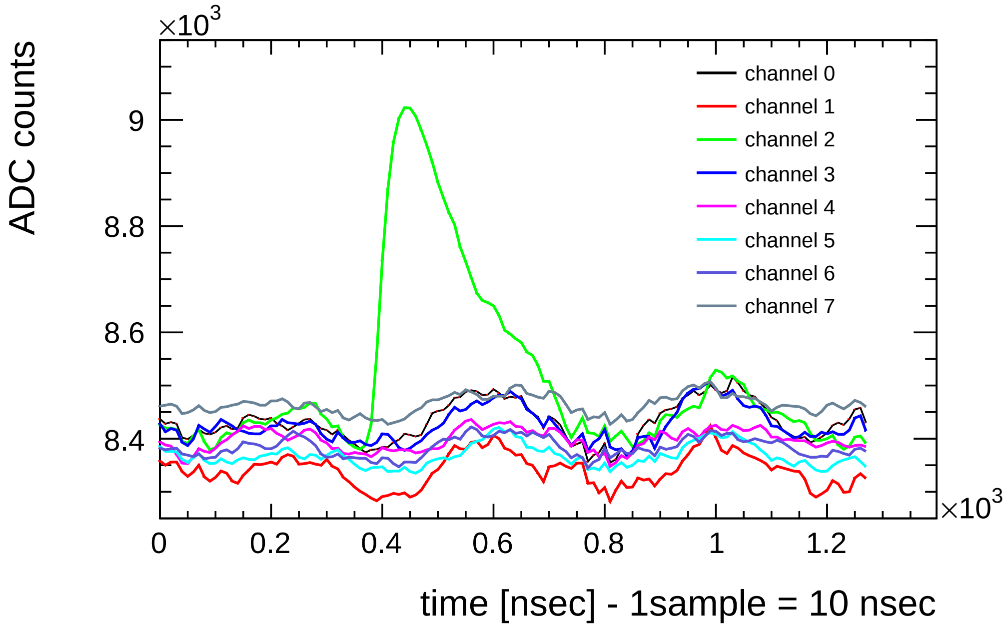

Figure 5.5: An example of an event record (run 99 event 46), each color represents one of the eight channel outputs.

to be matched off-line. To ensure the synchronization between the DAQs, a veto scheme (through BUSY signal) was used as shown in Fig. 5.6. This ensured that both DAQs acquired the same event and had the same number of events at the end of the run.

5.1.6 Data taking

Using the trigger logic described in subsection 5.1.5, sets of 50K events produced by a beam of 4.5 GeV electrons were recorded in each run (the analysis software for the telescope data could not handle larger amounts of data at the time). Two areas of the silicon-sensor were measured, eight pads in the outermost radius of sector L1 (area 1 of about $8 \times 1.8\,\mathrm{mm} \times 20\,\mathrm{mm}$) and eight pads in the innermost radius of sector L2 (area 2 of about $8 \times 1.8\,\mathrm{mm} \times 10\,\mathrm{mm}$), as shown in Fig. 5.7. Since the beam profile is $5\,\mathrm{mm} \times 5\,\mathrm{mm}$, and the larger pad area (area 1) is $\sim 288\,\mathrm{mm}^2$, 20 xy points were measured in order to cover the full area. Altogether around 1M triggers were collected for each area. Also a set of measurements to investigate the effect of high voltage on the sensor performance was taken. Measurements were also performed to study the response of the readout chain to electromagnetic showers, by adding blocks of

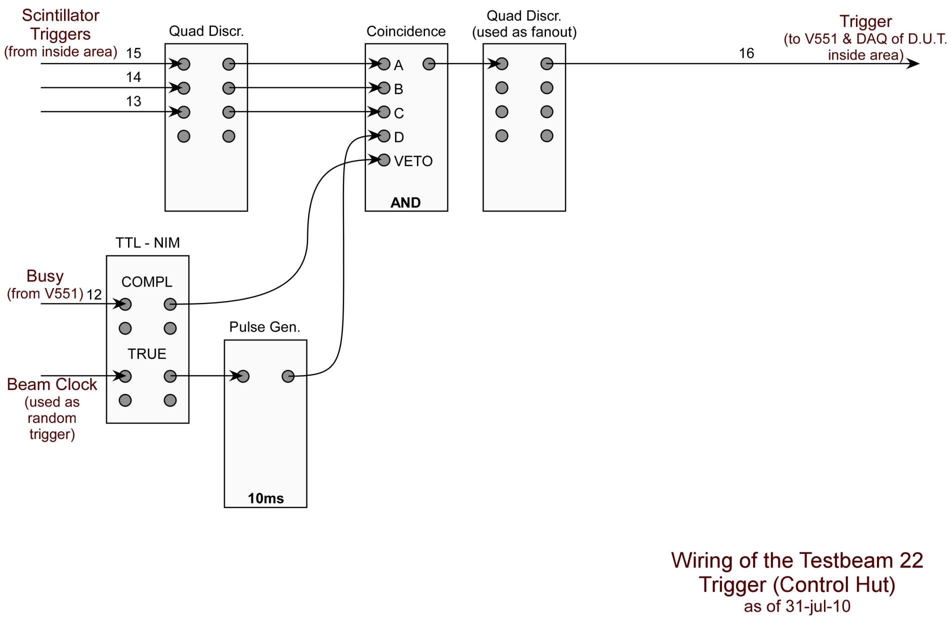

Figure 5.6: The connection scheme for the trigger logic.

tungsten (W) absorber in front of the sensor - these measurements will not be discussed in the present analysis.

5.2 Analysis of silicon-sensor data

The first part of the test beam data analysis is based on data recorded by the silicon-sensor DAQ.

5.2.1 Noise correlations

The type of multi-channel read-out electronics which was custom-designed for the silicon-sensor is known to generate correlated noise (common mode). This can already be seen in Fig. 5.5, where the 128 samples of an event in the eight read-out channels tend to oscillate in a coherent manner, around their individual base-line. In order to estimate the correlation coefficient between every two channels, one can use the following parameter defined for each

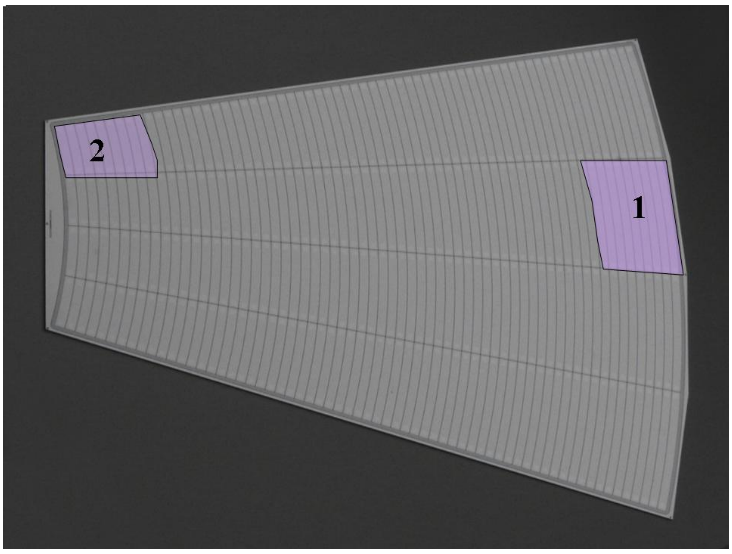

Figure 5.7: The two area of the silicon-sensor tile, area 1 and area 2, each consisting of eight pads, investigated in the beam tests.

event:

$$\rho_{i,j} = \frac{\langle S_i S_j \rangle - \langle S_i \rangle \langle S_j \rangle}{\sigma_i \sigma_j}, \tag{5.1}$$

where, $\langle S_i \rangle$, $\langle S_j \rangle$ are the averages over the 128 signal samplings in channel i and channel j of a single event; $\langle S_i S_j \rangle$ is the average product of the samplings and σ_i,σ_j are the RMS of the 128 samplings in channels i and j, respectively. This definition can only be applied to pairs of pads (channels) which where not traversed by the beam particle - empty channels (in Fig. 5.5 channel 2 would be excluded from the pairing). The distribution of $\rho_{i,j}$ for a particular pair of channels in area 2, for all events, is shown as an example in Fig. 5.8. The most probable value of $\rho_{i,j}$ is estimated at around 0.8. In Fig. 5.9, the most probable value (MPV) of the correlation coefficient for all pairs of channels is presented. The most probable value of about 0.7 only weakly depends on the pair of channels, suggesting the presence of a common mode noise. There is a tendency of the MPV for neighboring channels to be systematically lower than for other pairs, which may well be due to some bias in selecting 'empty' channels.

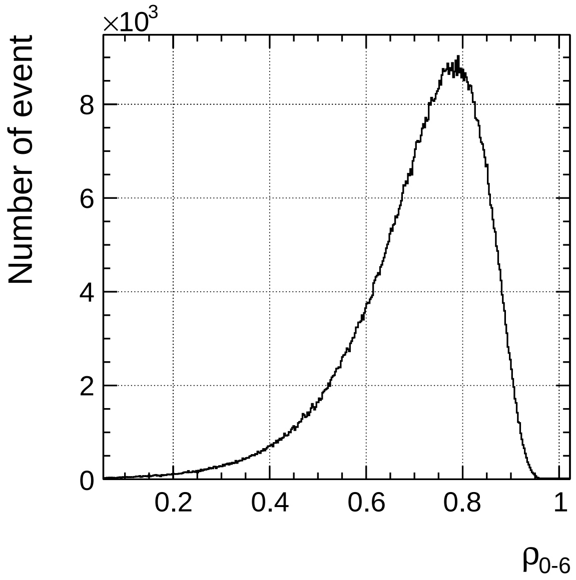

Figure 5.8: Distribution of the correlation coefficient $\rho_{i,j}$ for $i = 0$ and $j = 6$ in area 2 for the full data set.

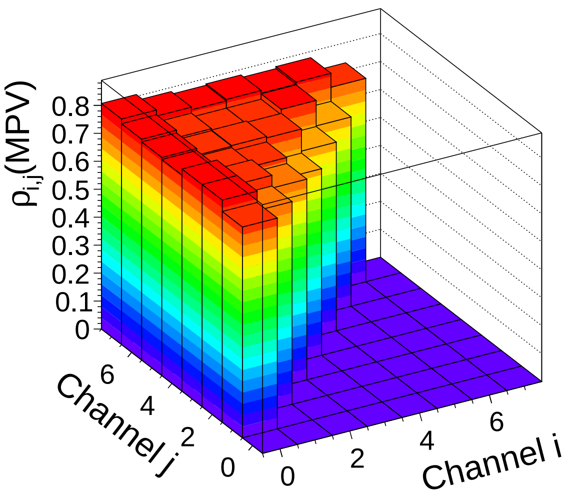

Figure 5.9: The most probable value correlation coefficient,$\rho_{i,j}(MPV)$ for all i, j pairs of channels.

5.2.2 Common mode filter

The extraction of the common mode noise from the raw data is done in several steps. First, the base-line for each channel is determined. The calculation of the base-line in each channel is performed by averaging each of the 128 samplings over the full data set. For each channel, only events that are part of the pedestal of the spectrum had been taken. The full base-line structure (128 points) calculated for the pads in area 1 can be seen in Fig. 5.10. The

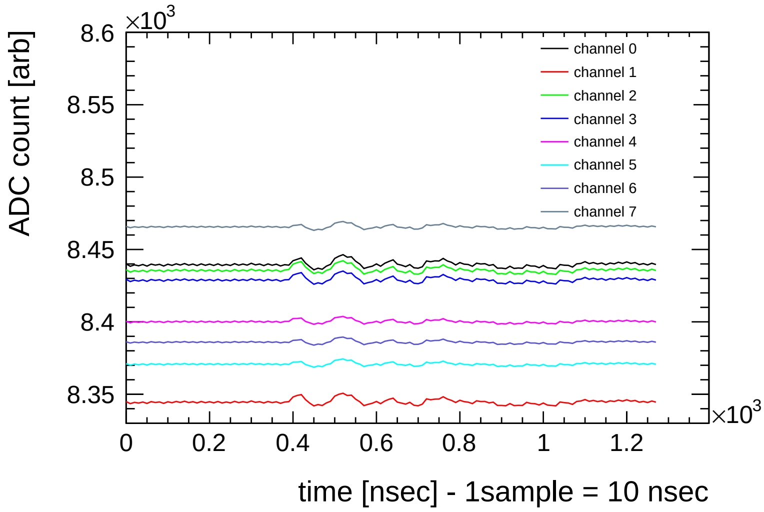

Figure 5.10: Base-line for all channels in area 1, after averaging each sampling, over the full dataset.

base-line is fairly constant over the 128 sampling points, with the exception of the range between sampling 40 and 80 where the beam related signal is expected, suggesting that the common mode is affected by the processing of the signal. However the fluctuations are at a percent level and will be ignored in this analysis.

The second step in extracting the common mode is to reduce the base-line level of the full event to zero by subtracting the average base-line sample by sample, channel by channel. The result of the subtraction is shown in Fig. 5.11 for one event, where the beam was crossing channel (pad) 1. The common mode is determined on an event by event basis. It is obtained by averaging each sampling over the empty channels. For example, for the event displayed in Fig. 5.11, the common mode is determined from seven channels (0,2,3,4,5,6,7), that is excluding channel 1 which was traversed by the beam. The result is shown in Fig. 5.12. The final result, after subtracting the common mode is shown in Fig. 5.13b, for the event of Fig. 5.11. For completeness, the event record before processing is also shown.

In reality, the procedure of determining a common mode in the present

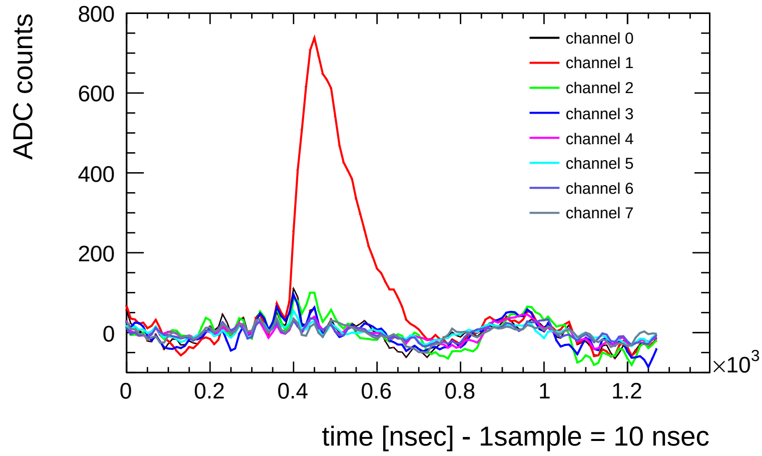

Figure 5.11: The profile of the 128 samplings of one event after subtracting the base-line in each of the eight channels. The beam traversed the pad of channel 1.

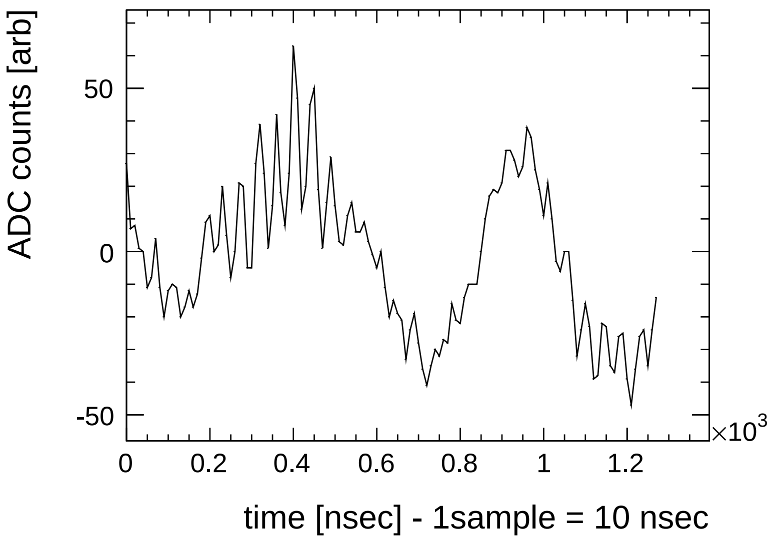

Figure 5.12:
The common mode for the event from Fig. 5.11

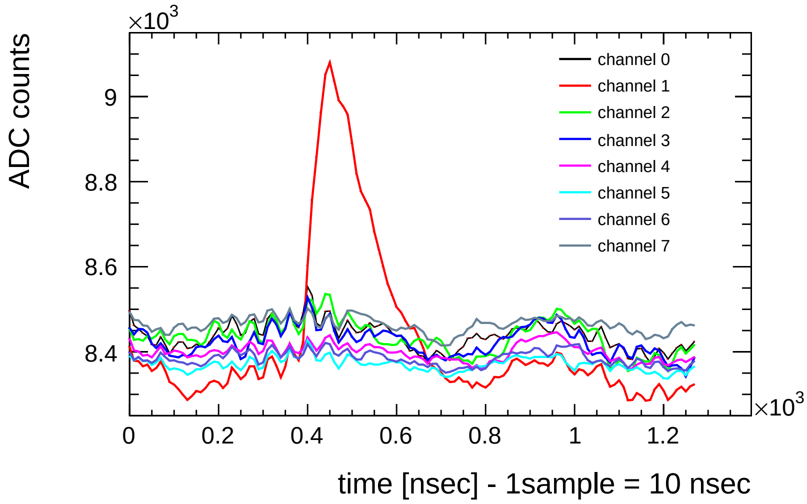

(a) A full event before filter

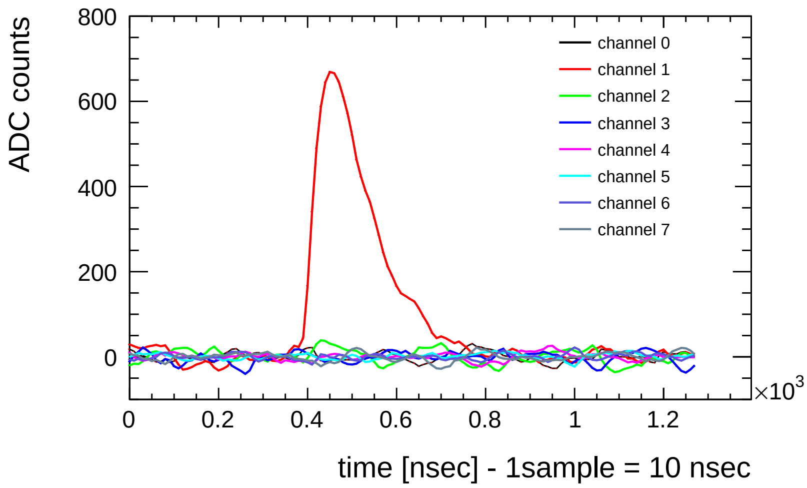

(b) A full event after filter

Figure 5.13: The sampling distribution of the eight channels of an event before - (a) and after - (b) subtracting the base-line and the common mode filter.

data set is complicated by the fact that the gains in the eight channels were different. Therefore in the averaging of channels one needs to keep track of the appropriate scale factors, which are determined by the most probable value of the real signal.

5.2.3 Temperature dependence

When determining the base-line, one needs to take into account its possible temperature dependence. In Fig. 5.14, the average over the first 30 samplings of an event, further averaged over the events in one physical run, is shown as a function of the average temperature recorded for that run. The temperature dependence is shown for all eight channels of area 2. A temperature change of 1° leads to a change of 20 ADCcounts in the base-line, independently of the channel. The typical size of one run was 50k events

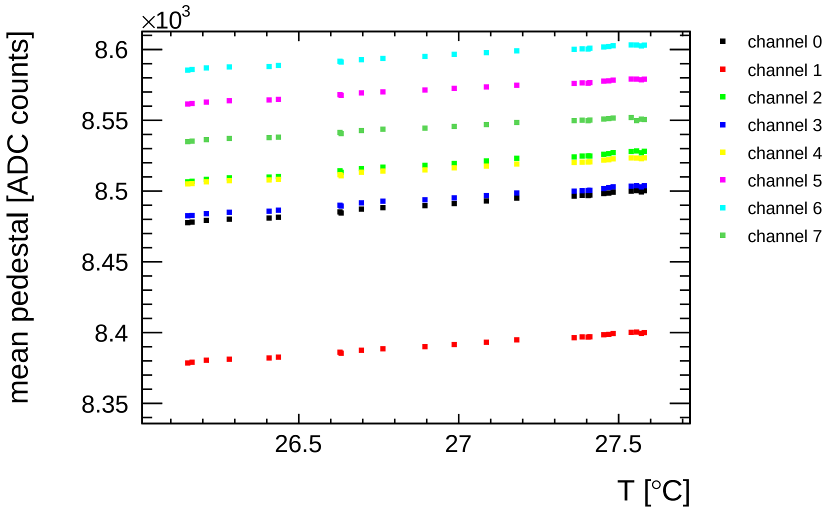

Figure 5.14: The mean value of the base-line as function of temperature, T.

collected during typically 15 to 20 min. During this period, the expected change in the base-line is of the order of 1 ADCcount.

The origin of this temperature dependence is most probably due to the properties of the ASICs. As discussed in subsection 4.2.3 the dark current of the reverse biased sensor has in principle a temperature dependence. However, since the various channels in area 2 have different gains, if the temperature dependence was due to the subsequent change of the dark current, different slopes for different channels would be expected which is not the case.

5.2.4 Spectrum analysis

In order to quantify the size of the signal in the sensor from the 128 samplings, several methods can be used.

One possibility is to determine the maximum amplitude, Q_{max}, within the 128 samplings per event per channel. This is the method which is planned for the LumiCal detector at the ILC. Only one reading is planned for each bunch crossing. The amplitude will be read at a specific time which would correspond to the expected maximum of the signal. This method minimizes the contribution of noise.

Another method consists of integration over several samplings. This measurement corresponds to the amount of charge measured by the ADC, Q_{int}. The number of samples used can by optimized for best S/N performance. For this analysis a window of 65 samples starting at the 35th sample was chosen as illustrated in Fig. 5.15. The wide shape and slow fall-off of the signal comes from the shaper in the ASIC that expands the narrow input signal from the sensor (1 ns) to a clear signal.

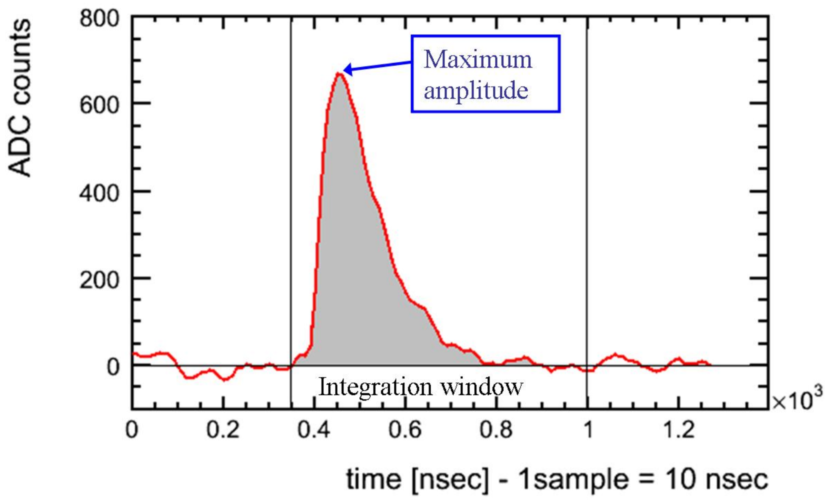

Figure 5.15: Illustration of the different methods to quantify the signal from the sensor after the fron-end electronics. The blue arrow marks the sampling location with maximum amplitude. The surface of the gray area under the red curve which outlines the sampling values denotes the integrated signal.

The two methods differ in resolution, S/N ratio and in the calibration constants. Examples of spectra obtained with the Q_{max} and the Q_{int} methods, without and with corrections for the common-mode, for all events collected in area 1, for a particular channel (channel 2) are shown in Fig. 5.16. Each spectrum consists of a peak centered around zero which corresponds to the pedestal and another broad bump which corresponds to the signal. The pedestal distribution originates from fluctuations of the electronic noise. Note that the ratio of events in the signal and the pedestal regions is determined by the percentage of data collected for channel 2 out of the full scan of area 1 (about 1/8). It is clear that the separation between the pedestal and the signal is much more pronounced after applying the common-mode filter as seen in (b) and in (d) compared to (a) and (c) without common-mode filter.

Each spectrum is fitted with a sum of one Gaussian for the pedestal region and the Landau distribution convoluted with the same Gaussian. The Landau distribution describes the energy loss of a charged particle in silicon. In general the fit reproduces the spectra very well, with the exception of the small area between the two maxima, the more visible the larger the separation between them. As will be explained in subsection 5.4.4, this has been identified as an edge effect, when the beam crosses the pad close to the gap region or the gap itself.

The signal to noise ratio, S/N, is defined by

$$S/N = \frac{MPV_{signal} - MPV_{pedestal}}{\sigma_{pedestal}}, \tag{5.2}$$

where the MPV_{signal} is the the most probable value (MPV) of the the fitted Landau distribution convoluted with the pedestal Gaussian, $MPV_{pedestal}$ is the mean of the fitted Gaussian and the $\sigma_{pedestal}$ is the standard deviation of the latter. The values of S/N for all the channels in both areas are summarized in Table 5.1. Also included in the Table are the estimated values of Q_{max} and Q_{int} from the fitted MPVs after subtracting the pedestal, without and with common-mode filtering. The S/N ratio is higher for the Q_{max}-method and the common-mode filter improves the ratio by more than factor 3 for the higher gain channels and by factor about 2.5 for the lower gain channels. In the Q_{int}-method filtering dramatically improves the S/N ratio hower it remains worse than in the Q_{max}-method.

5.3 Study of cross-talk

The cross-talk between channels is a phenomenon which causes a signal to appear in one channel as a result of activity in another channel. The cross-

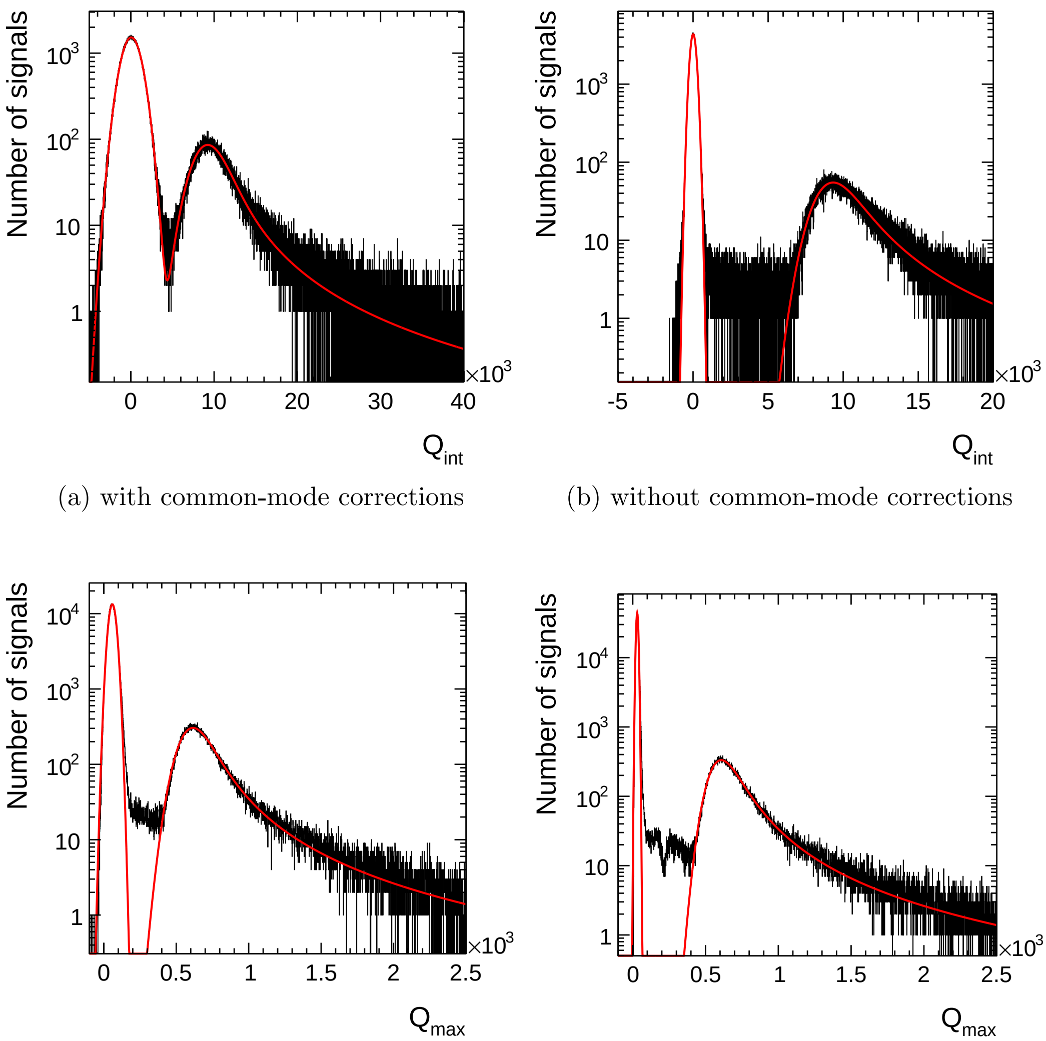

(a) with common-mode corrections (b) without common-mode corrections

(c) with common-mode corrections (d) without common-mode corrections

Figure 5.16: Distributions of the signal estimated with the integration method, Q_{int}, and with the amplitude method, Q_{max}, for channel 2 in area 1, without and with common-mode filter, as denoted in the figure. The data are shown as histograms and the results of fitting a function consisting of a Gauss and a Gauss-Landau convolution are shown by the red curve.

talk appears when there is common capacitance between channels, as for example the inter-pad capacitance in the sensor and the capacitance between lines in the fun-out. Cross-talk may also originate from the multi-channel ASICs.

Table 5.1: The most probable value of the signal, after subtracting the pedestal, for the Q_{max}-method, $\tilde{Q}_{max}$, and the Q_{int}-method, $\tilde{Q}_{int}$ and the corresponding signal to noise ratio S/N, before and after applying the common-mode filter, for all the channels of area 1 nd area 2.

		before filter				after filter			
Area	Channel	$\tilde{Q}_{int}$	S/N	$\tilde{Q}_{max}$	S/N	$\tilde{Q}_{int}$	S/N	$\tilde{Q}_{max}$	S/N
1	0	8758	7.4	529	20	9237	43	562	74
	1	8790	8.0	527	21	9095	48	554	79
	2	8619	7.7	529	21	9015	47	557	77
	3	8708	7.9	527	21	9102	48	557	78
	4	4368	7.5	268	21	4619	28	279	50
	5	4432	7.5	272	21	4701	30	283	52
	6	4405	7.4	269	20	4668	30	282	52
	7	4404	6.9	267	19	4623	32	283	56
2	0	8634	7.1	524	19	8879	43	542	83
	1	8129	7.2	515	20	8535	38	519	73
	2	8354	7.5	515	21	8545	38	523	75
	3	8282	7.6	512	21	8530	39	522	75
	4	4336	7.5	265	20	4514	31	271	63
	5	4321	7.6	265	21	4504	33	271	65
	6	4355	7.5	266	20	4527	33	272	65
	7	4362	6.4	266	17	4546	33	275	64

Bench tests of the read-out ASICs showed that cross-talk levels from the ASICs are low and of the order of 1% for the physics gain, and about 0.1% for the calibration gain, where the physics gain option is designed for electromagnetic showers and the calibration option is designed for minimum-ionizing particles. Monte Carlo simulations of the ASIC performance give similar levels [34].

In order to investigate the cross-talk between channels, the correlation between the responses of every pair of channels was investigated. The correlation was studied for the full data set, and for all samplings in the response. The magnitude of each sampling was corrected for the base-line and common-mode noise and will be denoted by Q_{sam}.

An example of the observed correlation between channel 1 and 2 of area 1 is shown in Fig. 5.17. One clearly observed three domains, the pedestal area around (0,0), and the two areas along each of the axes, where a real hit was found in one of the channels and no hit in the other one (pedestal).

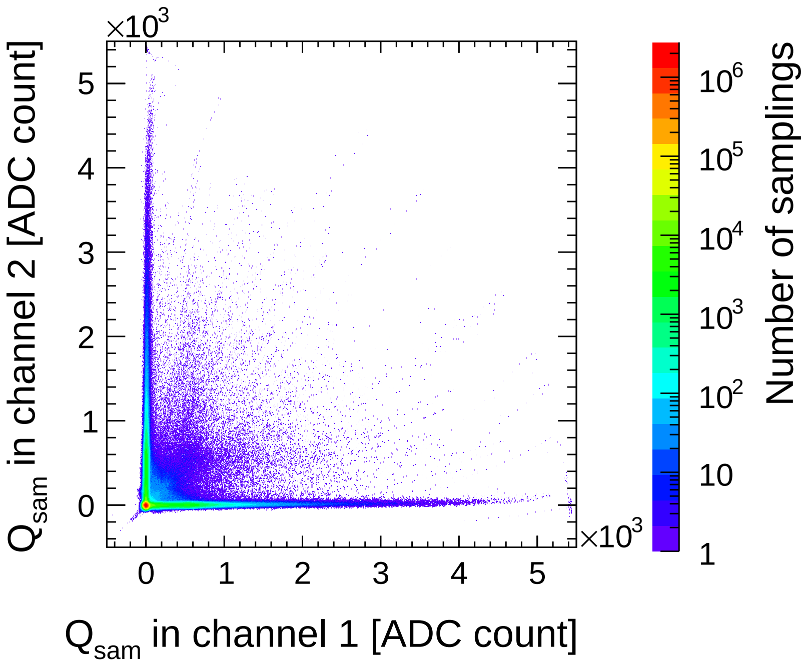

Figure 5.17: A correlation plot of sample magnitudes corrected for common-mode noise, Q_{sam}, in channels 1 and 2 in area 1, for all samplings in an event.

If there was no cross-talk between the channels, the area "parallel" to one of the axes would consist of a vertical or horizontal band with a width given by the pedestal of the other channel. In Fig 5.18a, the mean value of the pedestal in channel 2 is plotted as a function of the signal in channel 1 and the other way around in Fig 5.18b. The RMS of the distributions from which the average is calculated is plotted as the uncertainty. A clear dependence of the mean pedestal value of one channel on the response of the other is observed. The strange behavior observed in the mean pedestal value for small values of $Q_{sam}$is due to the special dependencies observed in the area close to (0,0) in Fig. 5.18 and will be discussed later.

After calibrating all channels through their MPVs, the cross-talk coefficient can be defined as the slope of the dependence of the mean pedestal

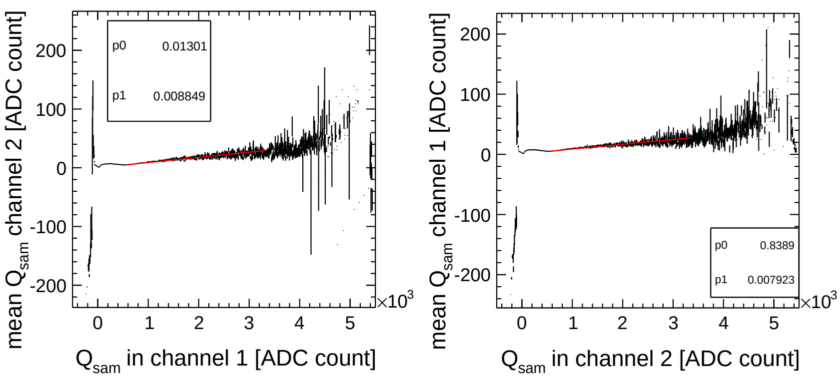

(a) (b)

Figure 5.18: The average response in channel 2 as a function of the response in channel 1 (a) and the other way around (b).

value of one channel on the response in the other channel. In order to determine the slope, a linear fit is performed from a response of Q_{sam}=1 MPV to Q_{sam}=6 MPV. The fit is performed for every pair of channels in each area and the results are summarized in Fig. 5.19. As expected the cross-talk is small, in percentage level, and is significant in neighboring channels. The observed cross-talk coefficient for the pads in area 2 (3%) is more than twice the value of the coefficient for the pads of area 1 (1%). This is probably due to the longer transition-lines from pads in area 2 to the ASICs than those from pads in area 1.

It is of interest to study in detail the area around (0,0) in the correlation plot of Fig. 5.18. A zoom-in of this area is shown in Figure 5.20. There is clear evidence that there is no correlations between the channel 1 and channel 2. This also means that the common-mode noise is properly accounted for.

5.4 Integration of positions and spectrum analysis

The sensor areas 1 and 2 were scanned with the beam by moving the DUT in the plane perpendicular to the direction of the beam. In this section, the response of the pads to the location of the beam is investigated. The response for each pad is measured in terms of $\tilde{Q}_{max}$. The impact point of the beam-particle on the sensor-pad is reconstructed from the data recorded by

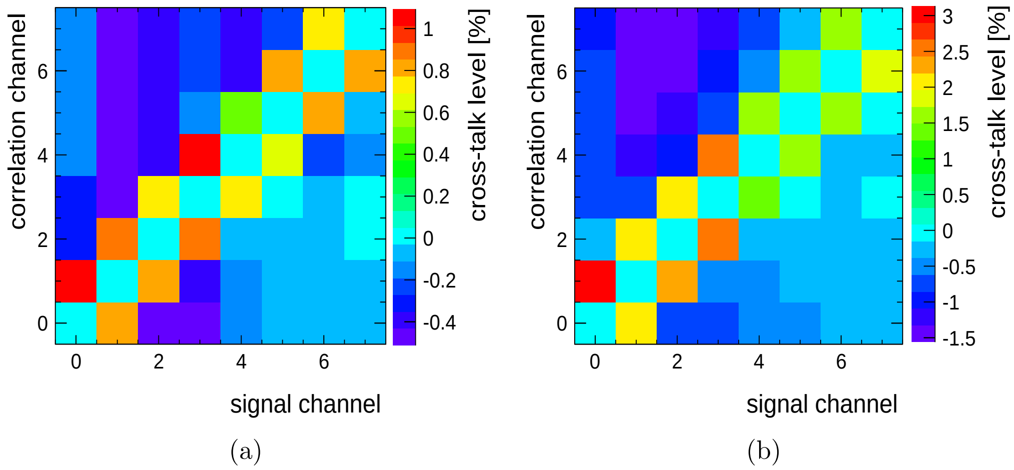

Figure 5.19: A map of the cross-talk coefficients between all channels in area 1 (a) and area 2 (b), expressed in percentage of the MPV.

the ZEUS MVD telescope.

5.4.1 Telescope alignment

The telescope readout pitch is 50 μm and the expected resolution in each plane is of the order of 28 μm [38]. Since the physical alignment of the sensor plane is of the order of mm, further alignment checks are needed. The relative alignment between plane 2 (plane 3) and plane 1 was determined from the $\Delta x_{2-1(3-1)} = x_{2(3)} - x_1$ and the $\Delta y_{2-1(3-1)} = y_{2(3)} - y_1$ distributions shown in Fig. 5.4.1. Shifts up to 1 mm are observed. Three out of the four distributions are Gaussian in shape. The Δy_{3-1} has distortions which are probably due to presence of a metal bar supporting the xy-table which acted as a collimator. The distributions were fitted with a Gaussian to determine the shifts between the planes. The shifts, summarized in Table 5.2, are then used in the track reconstruction.

Table 5.2: Summary of the alignment shifts determined for the ZEUS MVD telescope.

	plane 2	plane 3
x shift	$-150\,\mu$m	$676.5\,\mu$m
y shift	$101.7\,\mu$m	$-1322\,\mu$m

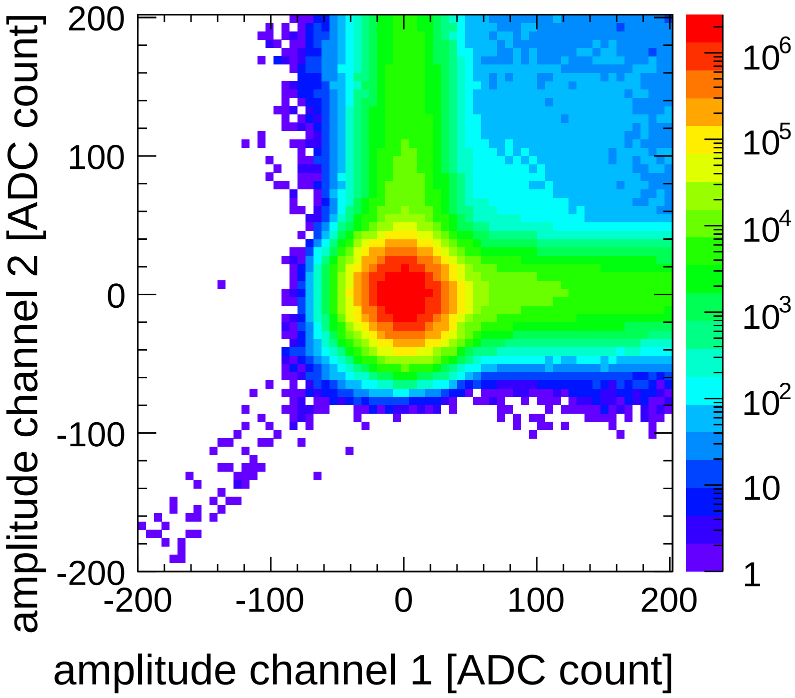

Figure 5.20: Zoom-in of the domain around (0,0) from Fig. 5.18.

5.4.2 Event reconstruction and synchronization

The beam particle trajectory was reconstructed by fitting a straight line to the positions recorded by the telescope in each of the three planes as a function of their z-position. To ensure the track accuracy, only tracks with one hit per plane and three hits in the telescope were reconstructed. This reduced the reconstruction efficiency to $\sim 52\%$. The telescope coordinate resolution was determined from the residuals of the fit. The residual distribution was then fitted with a Gaussian. The mean of the Gaussian was found to be compatible with zero within uncertainties and the σ values are listed in Table 5.3. They are found to be typically smaller than the inherent resolution, partly due to the selection bias.

The straight line was then propagated to the z-location of the sensor.

In this test-beam, the time stamping was critical since one needed to match between events recorded by the sensor-DAQ and the telescope-DAQ. We relied on the trigger/busy logic and low rate of events to determine that the two systems had the same number of events. The assumption was that

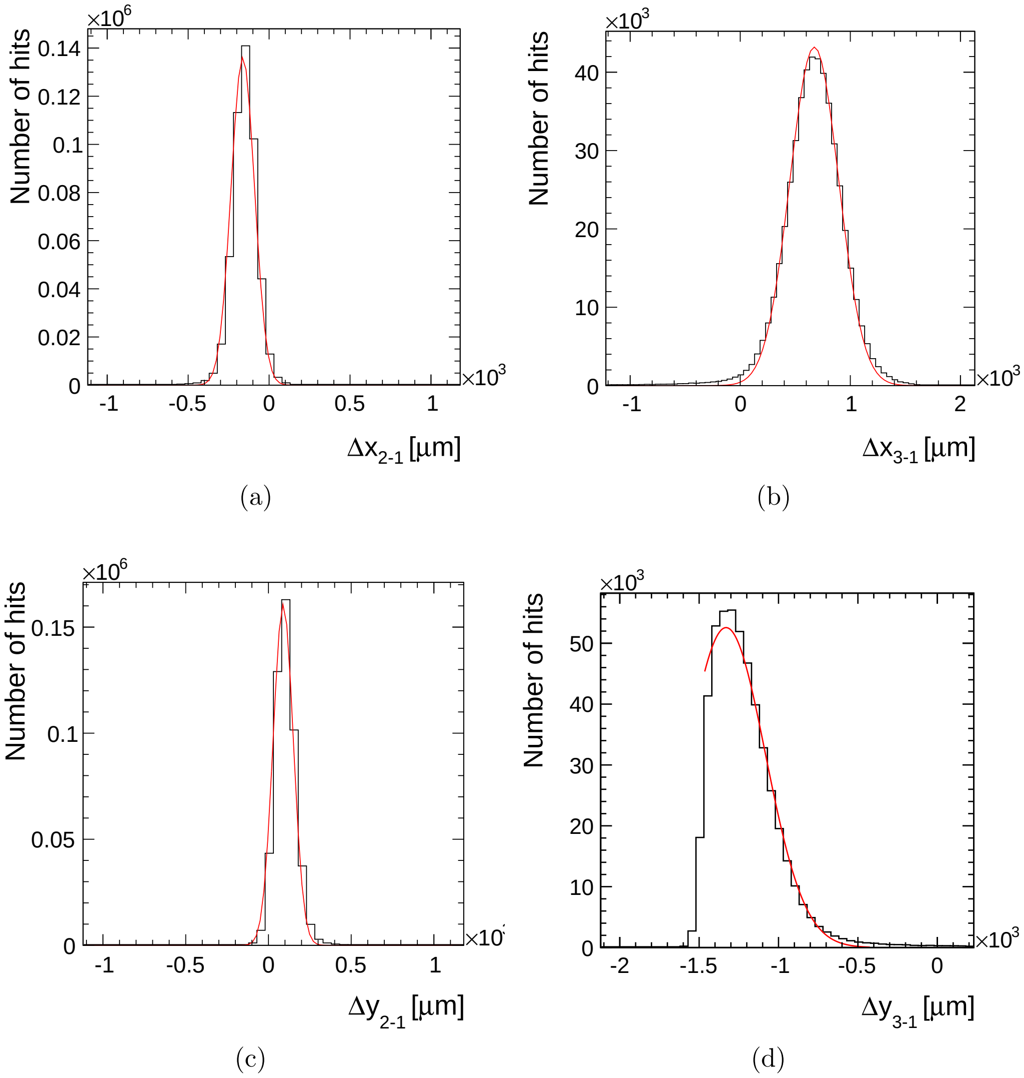

Figure 5.21: The difference between the coordinates of hits in planes 2 and 3 with respect to plane 1. (a) $\Delta x_{2-1} = x_2 - x_1$, (b) $\Delta x_{3-1} = x_3 - x_1$, (c) $\Delta y_{2-1} = y_2 - y_1$, and (d) $\Delta x_{3-1} = y_3 - y_1$.

the observed small difference in the number of events recorded came from the initialization sequence of the DAQ systems. Then, by skipping a small number of events in either data stream, the events could be matched and in the end all runs could be used. To determine the correct shift between the events in the two streams, for each run, the expected position in x and y on the face of the sensor was plotted with a color assigned to a particular pad. If the events were not properly matched, there was no observed patterns in the

Table 5.3: The x nd y resolution obtained from the σ of the Gaussian fitted to the residual distribution in the telescope.

	x resolution $[\mu m]$	y resolution $[\mu m]$
plane 1	14.7	14.6
plane 2	21.4	21.3
plane 3	6.9	7.0

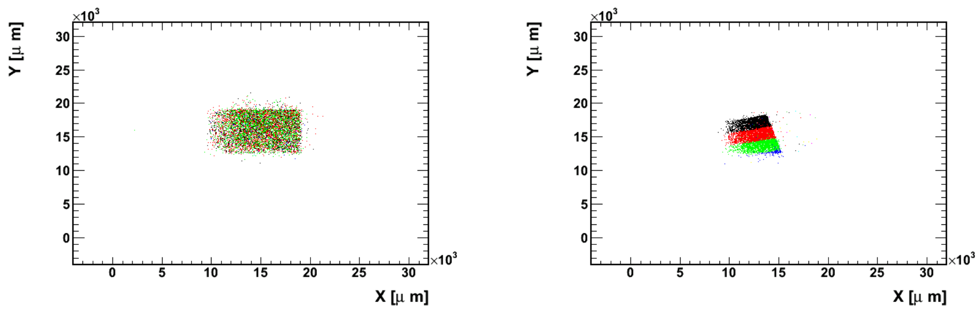

(a) (b)

Figure 5.22: y versus x of hits on the sensor surface. (a) hits for a sensor segment from data files which were not synchronized. (b) hits from the sensor segment after synchronization of data files.

colors as shown in Fig. 5.22a, while if the matching was correct the pattern shown in Fig. 5.22b would appear. In most cases a shit of up to 5 events would restore matching. The final matching, for all data sets from area 1, is shown in Fig. 5.23 where each of the eight colors represents one pad. The pad structure is very well reproduced. This is visualized by drawing the expected geometrical borders of the pads in the figure. In a small number of events and usually close to the edges of the pads, one observes displaced points which are due to the charge sharing effect and possibly also due to extra radiation.

5.4.3 Uniformity check

The response of the sensor was studied as a function of hit position, for area 1. To reflect the geometrical structure of the sensor, the expected hit position is transformed into the sensor design reference frame (see Fig 4.1), where $R = 0$ corresponds to the origin of the arcs that define the sensor

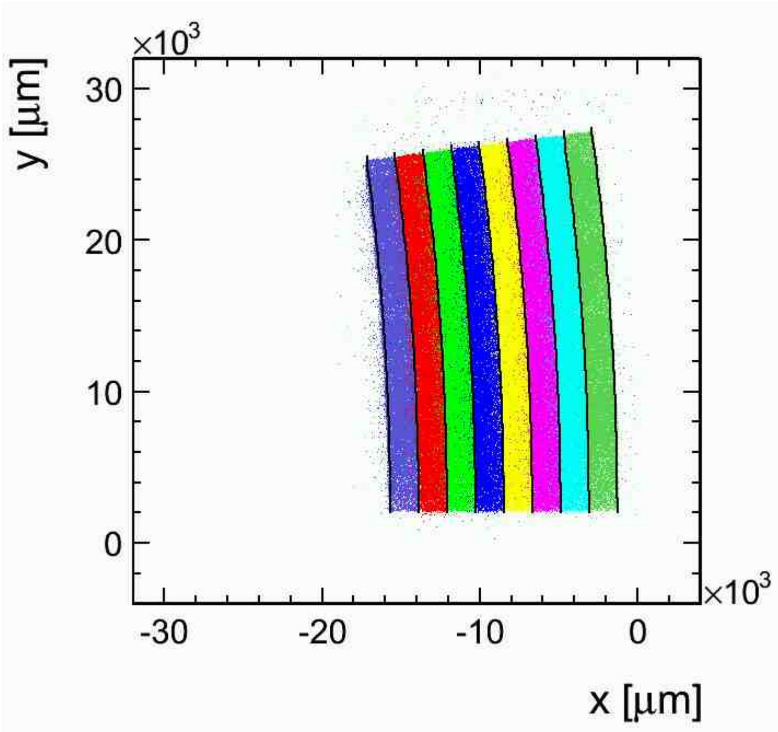

Figure 5.23: Full reconstructed data set of area 1. The colors represent the different channels and the black 7.5° arc represent boarders between pads. The coordinate system is arbitrary from the xy table, and represents a view from the beam origin on the sensor.

and the angle ϕ runs along the arcs. The radial distance span of area 1 was divided into 0.1 mm wide bins and in ϕ, 16 bins of 0.5° were defined. The response of each pad, Q_{norm}, was calibrated such that $Q_{norm} = Q_{max}/\mathrm{MPV}$ and for each expected position the sum over the eight pads in area 1 was determined, Q. The values of Q are thus expressed in terms of MIPs. The average Q as a function of R and ϕ is shown in Fig. 5.24. The pad structure is reproduced, with evident areas of lower response between the pads and in the sector edges ($\phi = 0$ and $\phi = 7.5°$). Inside the pads, the response is uniform at around 1.8 MIP, independently of the gain. The response in the edge areas is lower by about 10%.

In Fig. 5.25a, the contribution for each pad is shown as a function of R and in Fig. 5.25b the contribution of all pads is presented as a functio of R. The 10% decrease in the total charge collection is observed around the 0.1 mm gap between pads and the region extends thruogh about 0.2 mm. The contribution of pads which were not hit by the beam amounts to about

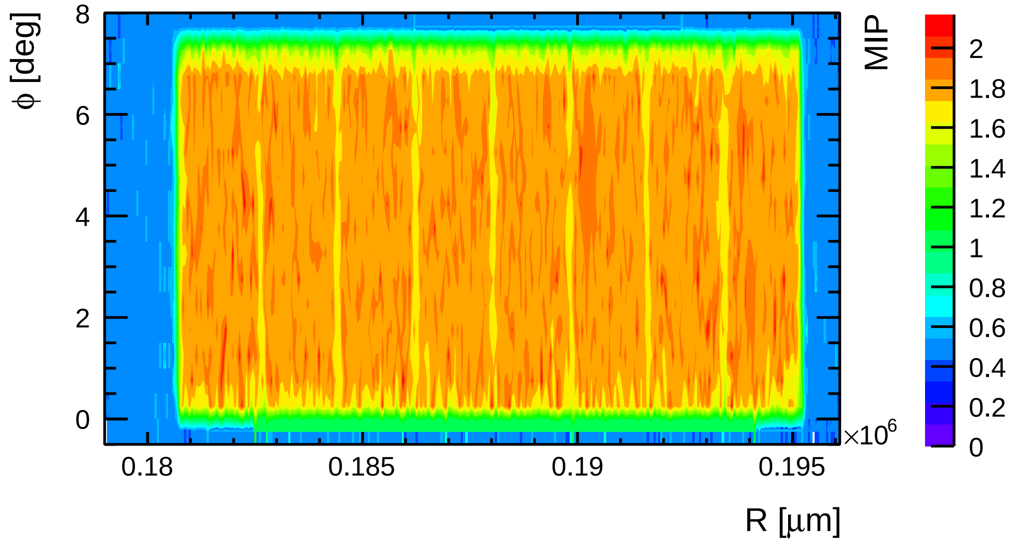

Figure 5.24: Mean collected response expressed in MIPs as a function of the angle ϕ and radial distance R.

20% of the signal, which demonstrates how important it is to subtract the pedestal in the Q_{max}-method. The non-uniformity is at the level of $< 1.5\%$, to be compared to $15\,\mu$m tolerance in the $320\,\mu$m of the sensor depth.

5.4.4 Charge sharing between pads

In Fig. 5.25a it is clearly seen that a substantial contribution to the response of a pad originates from neighboring pads. To further investigate this effects, each was subdivided into radial bins and the corresponding spectrum of Q_{max} was investigated. The pad area was divided radially into $200\,\mu$m segments. The two areas of $200\,\mu$m around the center of the pad gap ($-100\,\mu\text{m} \leq R \leq +100\,\mu\text{m}$) were also explored. An example of the spectra obtained in small radial bins for channel 1 in area 1 is shown in Fig. 5.26. When comparing Fig. 5.26 to the full spectrum as shown in Fig. 5.16), it becomes quite evident that the gap between the pedestal and the main signal is filled by events in which the beam particle hit the pad close to the gap edge. This is a result of charge sharing. Charge sharing is a result of a track that induces charge generation in two (or more) pads. This effect is to be expected to reduced when the operation voltage of the sensor is rising and will subject to tests in the next beam tests. In the spectrum integrated over the full pad area, the

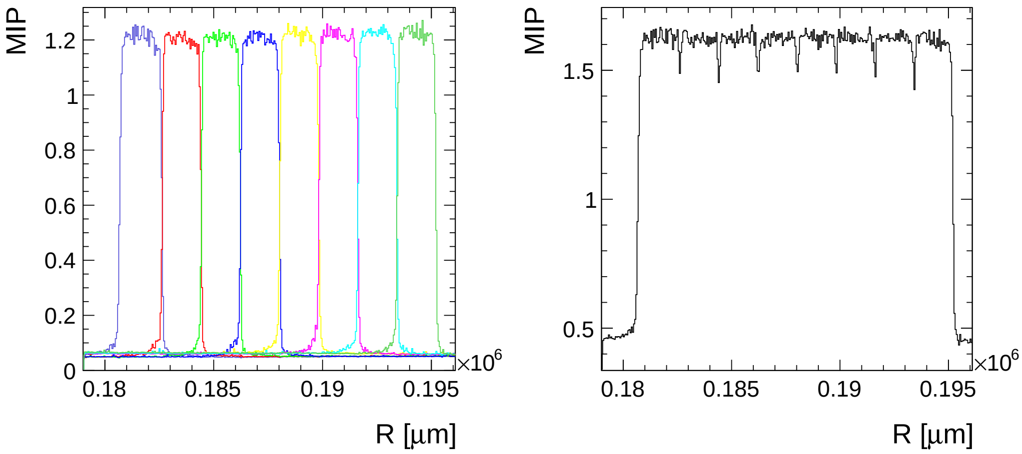

(a) (b)

Figure 5.25: (b) Mean collected response expressed in MIPs as a function of R separately for each pad identified by a different color. (c) Mean collected response expressed in MIPs as a function of R summed over all pads.

events that populate the gap between the pedestal and the signal constitute 5% of the signal events.

5.5 Conclusions

A full chain of the LumiCal sensor prototype equipped with read-out electronics was tested in the 4.5 GeV electron beam of DESY. Two selected areas, each consisting of eight pads, one in the inner most and one in the outer most sections of the sensor were investigated. The areas were scanned in the directions perpendicular to the beam. The response of the sensor was studied, including the contribution of the common-mode and the cross-talk between channels. Two different methods of quantifying the signal in the pad were investigated and the simplest method of selecting the maximum value of the 128 samplings of the shaped pulse in time was found to give the best signal to noise ratio, $S/N \simeq 70$. The uniformity response was extracted from the position dependence of the signal. A non-uniformity of about 1.5% was observed for beam particles well contained within the pad, well within the manufacturer's tolerance in depth of the sensor. The gap between pads leads to a 10% lower charge collection efficiency. The long tail of signals

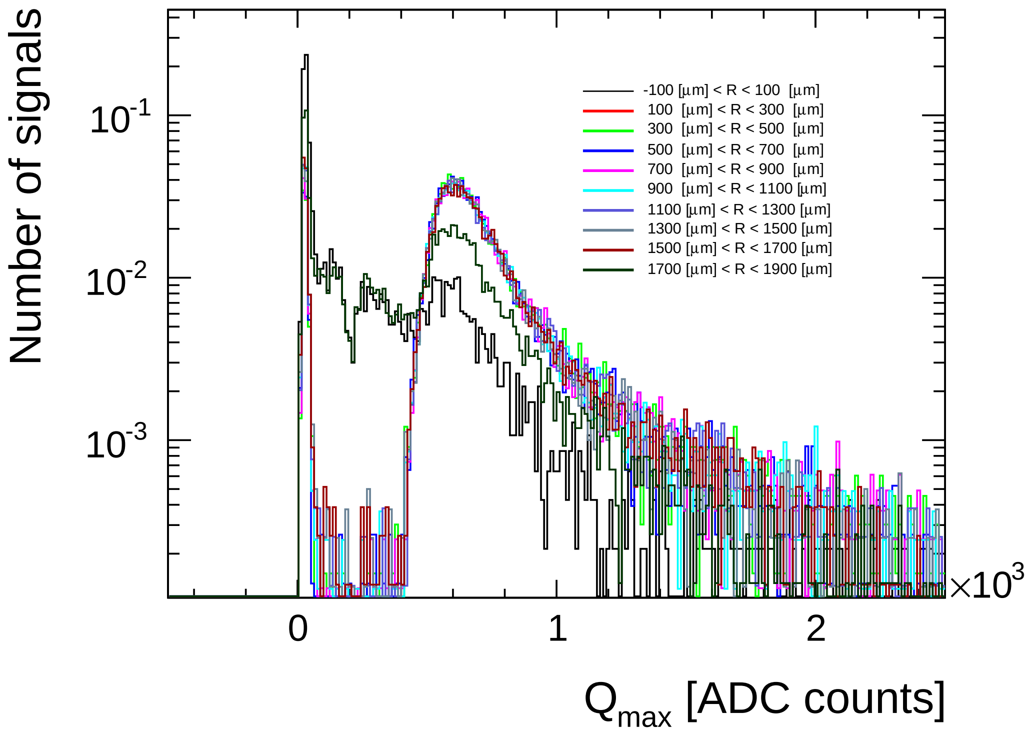

Figure 5.26: Distribution of Q_{max} in radial slices of pad 1 in area 1. The slices are described in the figure.

between the pedestal and the main signal was identified as originating from the charge-sharing phenomenon.

Summary

The design of the luminosity calorimeter (LumiCal) for a future linear collider is based on a tunsten-silicon sandwich calorimeter. The first prototype of the silicon sensor, produced by Hamamatsu, was tested and characterized in the newly set up silicon lab of Tel Aviv University. The results were found to be compatible with the ones obtained in the Cracow and Zeuthen advanced silicon labs. A sensor equipped with read-out electronics was tested in the 4.5 GeV electron beam of DESY. The results of this first beam-test are presented and indicate that the sensor properties are well understood and that the design of the front-end electronics is adequate. This is the first step in developing the prototype of LumiCal for precision measurements of the rate of Bhabha scattering events, which puts very stringent limits of the uniformity and stability of the silicon sensors. The results of this thesis constitute the first steps in designing the protocol for building he LumiCal prototype.

Acknowledgments

I would like to thank my supervisors, Prof. Halina Abramowicz and Prof. Aharon Levy, for a lot of things.

This work is partly supported by the Israeli Science Foundation.

Bibliography

[1] S. Dawson and M. Oreglia, “Physics opportunities with a tev linear collider,” *Annual Review of Nuclear and Particle Science*, vol. 54, no. 1, pp. 269–314, 2004, URL: http://www.annualreviews.org/doi/pdf/10.1146/annurev.nucl.54.070103.181259.

[2] L. Linssen, A. Miyamoto, M. Stanitzki, and H. Weerts, “Physics and Detectors at CLIC: CLIC Conceptual Design Report,” 2012. CERN-2012-003.

[3] Brau, James and Okada, Yasuhiro and Walker, Nicholas J. and Djouadi, Abdelhak and Lykken, Joseph and others, “International Linear Collider reference design report. 1: Executive summary. 2: Physics at the ILC. 3: Accelerator. 4: Detectors,” 2007. ILC-REPORT-2007-001, AAI-PUB-2007-002, BNL-79150-2007, CERN-2007-006, CHEP-A07-001, CLNS-07-1991, COCKCROFT-07-04, DESY-07-046, FERMILAB-TM-2382, JAI-2007-001, JINR-E9-2007-039, JLAB-R-2007-01, KEK-REPORT-2007-2, LBNL-62867, LNF-07-9-NT, SLAC-R-857.

[4] K. Nakamura *et al.*, “Review of particle physics,” *J.Phys.G*, vol. G37, p. 075021, 2010. FERMILAB-PUB-10-665-PPD.

[5] ATLAS-Collaboration, “Combined search for the Standard Model Higgs boson using up to 4.9 fb-1 of pp collision data at sqrt(s) = 7 TeV with the ATLAS detector at the LHC,” 2012, 1202.1408. CERN-PH-EP-2012-019.

[6] A. Djouadi, “The Anatomy of electro-weak symmetry breaking. I: The Higgs boson in the standard model,” *Phys.Rept.*, vol. 457, pp. 1–216, 2008, hep-ph/0503172. LPT-ORSAY-05-17.

[7] S. P. Martin, “A Supersymmetry primer,” 1997, hep-ph/9709356.

[8] E. Elsen, M. Harrison, L. Hesla, M. Ross, P. Royole-Degieux, *et al.*, "International Linear Collider (ILC): A technical progress report," ANL-11-09, BNL-94832-2011, IRFU-11-60, CERN-ATS-2011-004, COCKCROFT-11-01, CLNS-11-2076, DESY-11-041, IHEP-ILC-2011-1, ILC-HIGRADE-REPORT-2011-001, ILC-REPORT-2011-030, LNF-11-2(NT)-30-03-2011, JAI-2011-001, JINR-E9-2011-32, JLAB-R-2011-01, KEK-REPORT-2011-1, KNU-CHEP-ILC-2011-1, LLNL-TR-477656, SLAC-R-965.

[9] "Ilc images and graphics." URL: http://www.linearcollider.org/about/Press/Images-and-graphics.

[10] R. Heuer *et al.*, "Parameters for the Linear Collider." URL: http://www.fnal.gov/directorate/icfa/para-Nov20-final.pdf, 2003.

[11] A. Matoga, "Development of data acquisition system for luminosity detector at international linear collider," Master thesis, 2011.

[12] H. Schmickler, P. Lebrun, N. Toge, N. Phinney, T. Garvey, and P. Burrows, "A multi-tev linear collider based on clic technology: Conceptual design report." URL: http://project-clic-cdr.web.cern.ch/project-CLIC-CDR/CDR_Volume1.pdf, 2012.

[13] T. I. C. Group, "The International Large Detector: Letter of Intent," 2010, 1006.3396. DESY-2009-87, FERMILAB-PUB-09-682-E, KEK-REPORT-2009-6.

[14] E. Aihara, H., E. Burrows, P., E. Oreglia, M., E. Berger, V. Guarino, *et al.*, "SiD Letter of Intent," 2009, 0911.0006. Letter of Intent for SiD detector concept presented to ILC IDAG.

[15] A.M. Thomson, "Particle flow calorimetry and the pandorapfa algorithm," *Nuclear Instruments and Methods in Physics Research Section A: Accelerators, Spectrometers, Detectors and Associated Equipment*, vol. 611, no. 1, pp. 25 – 40, 2009.

[16] J. Aguilar-Saavedra *et al.*, "TESLA: The Superconducting electron positron linear collider with an integrated x-ray laser laboratory. Technical design report. Part 3. Physics at an e+ e- linear collider," 2001, hep-ph/0106315. SLAC-REPRINT-2001-002, DESY-01-011, DESY-2001-011, DESY-01-011C, DESY-2001-011C, DESY-TESLA-2001-23, DESY-TESLA-FEL-2001-05, ECFA-2001-209.

[17] k. Moenig, "Physics needs for the forward region," AUG 2004. Talk given at the FCAL Meeting, Zeuthen.

[18] "Fcal collaboration." URL: http://fcal.desy.de/.

[19] C. Grah and A. Sapronov, "Beam parameter determination using beamstrahlung photons and incoherent pairs," *Journal of Instrumentation*, vol. 3, no. 10, p. P10004, 2008.

[20] P. Bambade, V. Drugakov, and W. Lohmann, "The Impact of BeamCal performance at different ILC beam parameters and crossing angles on tau searches," *Pramana*, vol. 69, pp. 1123–1128, 2007, physics/0610145. LAL-06-145.

[21] Y. SATO, "Study of pair-monitor for ild," in *Proceedings of the Workshop of the Collaboration on Forward Calorimetry at IlC* (I. Bozovic-Jelisavcic, ed.), pp. 95–98, INN VInca, 2008. URL: http://www.vin.bg.ac.rs/hep/pub/FCAL_Belgrade.pdf.

[22] H. Abramowicz, R. Ingbir, S. Kananov, and A. Levy, "A luminosity detector for the International Linear Collider," 2007. LC-DET-2007-006.

[23] H. Abramowicz *et al.*, "Forward Instrumentation for ILC Detectors," *JINST*, vol. 5, p. P12002, 2010, 1009.2433. DESY-10-142.

[24] E. J.Bwocki, W.Daniluk and others., "Silicon Sensors Prototype for LumiCal Calorimeter," Dec 2009. EUDET-Memo-2009-07.

[25] M. Bergholz, "I/v and c/v measurements on hamamatsu si - detectors," Jun 2009. FCAL Meeting, Zeuthen.

[26] M. Green, "Intrinsic concentration, effective densities of states, and effective mass in silicon," *Journal of Applied Physics*, vol. 67, no. 6, pp. 2944–2954, 1990. cited By (since 1996) 143.

[27] A. Cerdeira and M. Estrada, "Analytical expressions for the calculation of pixel detector capacitances," *Nuclear Science, IEEE Transactions on*, vol. 44, pp. 63 –66, feb 1997.

[28] H. Spieler, *Semiconductor detector systems*. Series on semiconductor science and technology, Oxford University Press, 2005.

[29] G. Bolla, D. Bortoletto, R. Horisberger, R. Kaufmann, T. Rohe, *et al.*, "Sensor development for the CMS pixel detector," *Nucl.Instrum.Meth.*, vol. A485, pp. 89–99, 2002.

[30] N. Demaria, S. Albergo, M. Angarano, P. Azzi, E. Babucci, *et al.*, "New results on silicon microstrip detectors of CMS tracker," *Nucl.Instrum.Meth.*, vol. A447, pp. 142–150, 2000.

[31] L. Rossi, *Pixel detectors: from fundamentals to applications.* Particle acceleration and detection, Springer, 2006.

[32] S. Kulis *et al.*, "Test beam studies of the LumiCal prototype," Dec 2010. EUDET-Memo-2010-09.

[33] O. Novgorodova *et al.*, "Forward calorimeters for the future electron-positron linear collider detectors," *PoS*, vol. QFTHEP2010, p. 030, 2010.

[34] M. Idzik, S. Kulis, and D. Przyborowski, "Development of front-end electronics for the luminosity detector at ilc," *Nuclear Instruments and Methods in Physics Research Section A: Accelerators, Spectrometers, Detectors and Associated Equipment*, vol. 608, no. 1, pp. 169 – 174, 2009.

[35] U. Koetz, "Test of silicon strip detectors for the zeus microvertex detector," *Nuclear Instruments and Methods in Physics Research Section A: Accelerators, Spectrometers, Detectors and Associated Equipment*, vol. 461, no. 1-3, pp. 210 – 212, 2001. 8th Pisa Meeting on Advanced Detectors.

[36] C. Colledani, W. Dulinski, R. Turchetta, F. Djama, A. Rudge, and P. Weilhammer, "A submicron precision silicon telescope for beam test purposes," *Nuclear Instruments and Methods in Physics Research Section A: Accelerators, Spectrometers, Detectors and Associated Equipment*, vol. 372, no. 3, pp. 379 – 384, 1996.

[37] V. Kulibaba, N. Maslov, and S. Naumov, "Readout electronic for multichannel detectors," *Vopr. At. Nauki Teh., Ad.-Fiz. Issled.*, vol. 5, pp. 177–179, 2001.

[38] L. Bauerdick, E. Borsato, C. Burgard, T. Carli, R. Carlin, *et al.*, "Beam test of silicon strip sensors for the ZEUS micro vertex detector," *Nucl.Instrum.Meth.*, vol. A501, pp. 340–358, 2003, hep-ex/0212037.